

Review of MXene electrochemical microsupercapacitors

Qiu Jiang^{a,b,1}, Yongjiu Lei^{a,1}, Hanfeng Liang^a, Kai Xi^c, Chuan Xia^{d,*}, Husam N. Alshareef^{a,*}

^a Materials Science and Engineering, Physical Science and Engineering Division, King Abdullah University of Science and Technology (KAUST), Thuwal, 23955–6900, Saudi Arabia

^b Department of Engineering, University of Cambridge, Cambridge, CB2 1PZ, United Kingdom

^c Department of Materials Science and Metallurgy, University of Cambridge, Cambridge, CB3 0FS, United Kingdom

^d Department of Chemical and Biomolecular Engineering, Rice University, Houston, TX, USA



ARTICLE INFO

Keywords:

MXene
Microsupercapacitor
Fabrication techniques

ABSTRACT

The rapid development of miniaturized and wearable electronics has stimulated growing needs for compatible miniaturized energy storage components. Owing to their unlimited lifetime and high-power density, miniaturized electrochemical capacitors (microsupercapacitors) are considered to be an attractive solution for the development of these microelectronics, but they often depend on the choice of electrode materials and fabrication protocols for scalable production. Recently, a new family of two-dimensional transition metal carbides, carbonitride and nitrides (referred to as MXenes) has shown great promise in advanced microsupercapacitors with high energy and power densities. This was achieved thanks to the high pseudocapacitance, metallic conductivity and ease of solution processing of MXene. In this review, recent progress on MXene synthesis, microstructure design, and fabrication strategies of MXene microsupercapacitors are discussed, and their electrochemical performance is summarized. Further, we briefly discuss the technical challenges and future directions.

1. Introduction

The advent of fifth-generation (5G) communication in the fourth industrial revolution has fostered widespread research interest in the Internet of Things (IoTs) and sensor networks [1]. In these applications, a vast diversity of heterogeneous microsensors can connect and communicate with each other without network latency, disrupting various fields such as environmental monitoring, radio frequency identification, wearable electronics, and personal health care. Given these ubiquitous microsensors are usually discrete nodes that operate in independent wireless manners and sometimes are embedded in the human body, it is highly desirable to develop maintenance-free micro-/nano-scale power modules that are compatible with them.

One promising solution is to develop distributed energy sources that harvest energy from renewable sources such as solar, wind, thermal, or mechanical triggering/vibration [2,3]. To formulate such self-powered power units, an energy storage device is regarded as an essential short-term accumulator that captures charge from energy harvesting devices when microsensors are in stand-by mode and deliver continuous power to these microsensors when they are active. Microbatteries or thin-film batteries that store energy by the chemistry of lithium-ion

intercalation are the most popular choice as the miniaturized power source [4], but they suffer from their limited lifetime and low power density, which means periodic maintenance and replacement need to be carried out. Besides, the low power density also limits their use in some applications where a high spike of current is required [5].

As an alternative to batteries, electrochemical capacitors (ECs), also known as supercapacitors, are energy storage devices that store charge by adsorption of electrolyte ions onto the surface of electrode materials or by pseudocapacitive faradaic reactions (between the surface of the electrode material and the ions in the electrolyte). The energy density of ECs is relatively low as compared with batteries, but still can be sufficient to power various electronics for hours (Fig. 1). An electrochemical capacitor has a theoretically unlimited lifetime ($>10^5$ cycles) and delivers higher power densities as compared with batteries, which renders them better candidates as the energy storage component for microelectronics.

However, conventional ECs are too large for the microdevices, and the assembly methods of conventional supercapacitors are not compatible with the fabrication techniques in the microelectronic industry; this reality has fostered a great interest in the miniaturization of supercapacitors. The term “microsupercapacitor (MSC)” has been adopted to

* Corresponding authors.

E-mail addresses: Chuan.Xia@rice.edu (C. Xia), husam.alshareef@kaust.edu.sa (H.N. Alshareef).

¹ Contributed equally.

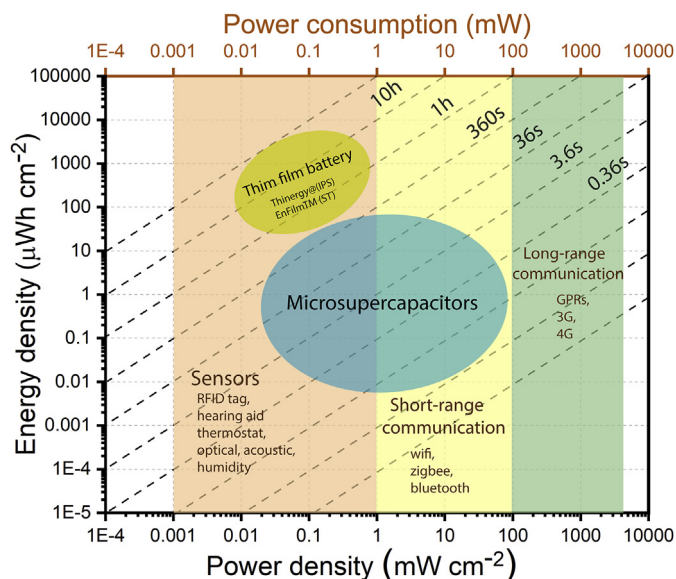


Fig. 1. Ragone plot showing energy and power densities of state-of-the-art microsupercapacitors. The vertical shaded area shows the power consumption of different electronics (corresponding to the top axis). The power density in the Ragone plot can be directly used to estimate practical electronic applications, given the area of the energy storage device is 1 cm^2 .

describe the supercapacitor devices which can be promisingly integrated with microelectronics, and it comes mainly in two flavors: thin-film electrodes with sandwich structure (thickness $< 10 \text{ }\mu\text{m}$) or arrays of planar microelectrodes with microscale sizes in at least two dimensions [5,6]. The concept of MSC has recently been further extended to fiber-based electrodes with core-shell structure [7–9]. Among these architectures, the in-plane interdigital design offers a multitude of advantages over the others because of its shorter ion diffusion distance, more substantial exposure of the electrode materials to the electrolyte, and the ease of integration with other microelectronics.

Porous carbons with high surface areas have been widely used for the fabrication of the microsupercapacitors, these include carbide-derived carbon [10], onion-like carbon [11], activated carbon [12], photoresist-derived carbon [13–16], carbon nanotubes (CNTs) [17–19], graphene [20,21], and laser scribed graphene [22]. Although these devices benefit from the high conductivity and large surface areas of the electrode material, they also deliver low energy densities as carbon materials store charges only through the adsorption of ions in the electrolyte. In order to overcome the low energy density limitations while maintaining high power densities, pseudocapacitive materials including conducting polymers [23–26], transition metal oxides (RuO_2 , MnO_2 , MoO_3 , Nb_2O_5 , VN) [27–33], black phosphorous (BP) [34], Conductive 2D metal-organic frameworks (MOFs) [35] and transitional metal dichalcogenides [36] have been explored for the fabrication of the microsupercapacitor devices. However, the poor electronic conductivity of metal oxides/hydroxides and MOFs may lead to mediocre power and cycling performance.

Recently, a large group of early transition metal carbides, nitride or carbonitride (MXenes) have been identified as a new class of two-dimensional (2D) materials [37]. The general formula of MXene is $\text{M}_{n+1}\text{X}_n\text{T}_x$, where M stands for an early transition metal (Ti, Mo, Cr, Nb, V, Sc, Zr, Hf or Ta), X represents carbon or nitrogen, n is usually an integral number between 1 and 3, and T_x is the surface termination such as hydroxyl, oxygen or fluorine. These surface terminations render the hydrophilicity of MXenes and also have a significant influence on their Fermi level density of the states, thereby electronic properties [38,39]. MXenes are synthesized by selectively removing the “A” layer from their

parent MAX phases, and “ene” was added to the last to show its 2D nature that is similar to graphene. Since its discovery in 2011 [40], MXenes have been particularly attractive as electrode materials for energy storage applications because of their unique structures including: (1) the inner conductive transition metal carbide layer that enables efficient electron transportation; (2) a transitional metal oxide-like surface that acts as active sites for fast redox reactions. Although there are more than 20 different MXenes that have been synthesized [41–44], most research to date has been focused on titanium carbide (Ti_3C_2) for MSC application due to its ultrahigh conductivity ($2.4 \times 10^4 \text{ S cm}^{-1}$) [45] and volumetric capacitance (1500 F/cm^3) along with ultra-high rate capability (10 V/s) in acidic media [46]. Besides their high volumetric capacitance, MXenes are particularly favorable for MSCs because of their 2D nature, which enhances the mechanical stability and shortens the ion diffusion paths between the positive and negative electrodes [47]. In this review, we present the latest developments in MXene-based microsupercapacitors, including electrode material design, different deposition/patterning techniques, and device architecture. Finally, challenges and perspectives of MXene-based MSCs are discussed.

2. Primary structure and evaluation metrics of microsupercapacitors

A conventional supercapacitor consists of a positive electrode and a negative electrode physically separated by a separator or solid-state ionic conductive electrolyte. The energy and power performance of the conventional supercapacitor is generally normalized by mass or volume of the electrode material, as the final user of these supercapacitors ranges from a sizeable load-leveling crane or engine starter to personal mobile devices. Differently, microsupercapacitors are designed to be the power source for microsensors, micromechanical systems, or wearable electronics that operate with low power consumption (milliwatts to microwatts). For these applications, the weight of active materials only takes a small part of the substrate and the whole device, thus normalizing energy and power density in a given footprint area (mWh/cm^2 , W/cm^2) are more practical to evaluate the performance of MSCs over gravimetric and volumetric performance metrics [5].

The first reported MSC was inspired by the technology from microbatteries [48,49], which utilizes a stacked configuration with solid-state lithium conducting electrolyte (lithium phosphorus oxynitride, LiPON) and sputtered RuO_2 electrode materials (Fig. 2a). The sandwich structure is considered to be the most effective architecture regarding the occupied surface area ($C_{\text{cell}} = \frac{1}{2} C_{\text{electrode}}$). However, regular ceramic electrolyte shows low ionic conductivity ($< 5 \text{ }\mu\text{S cm}^{-1}$) and poor wettability with the electrode, thus these primary devices show low specific capacitance and power density [3]. On the other side, solid-state or gel-type electrolytes are promising choices for leakage-free devices, but depositing electrode materials on liquid and gel electrolytes by vacuum deposition procedures is not practical. Instead, placing both positive and negative electrodes in the same plane is a more practical configuration. In the in-plane design, both sides of the electrodes occupy separate substrate area, and there are always inactive gaps between the electrodes, cell capacitance is thus less than one-fourth of the electrode areal capacitance ($C_{\text{cell}} < \frac{1}{4} C_{\text{electrode}}$). Simple interdigital finger electrodes (Fig. 2b) are the most commonly used in-plane design so far, while attempts have also been made to enhance the areal capacitance by mathematically derived fractal patterns [50]. As the areal performance of microsupercapacitors is limited by the mass of the active electrode layer, three-dimensional (3D) planar MSC having anodes and cathodes with surfaces exposed in all three dimensions instead of the planar surface of conventional thin-film electrodes were also established (Fig. 2c). The porous 3D structures can act as a mechanically reinforced framework and hence facilitate the transport of electrons, ensuring simultaneously both high capacitance and high-power density.

Microsupercapacitors are considered to be miniaturized supercapacitors; thus, the charge storage mechanism and basic calculation

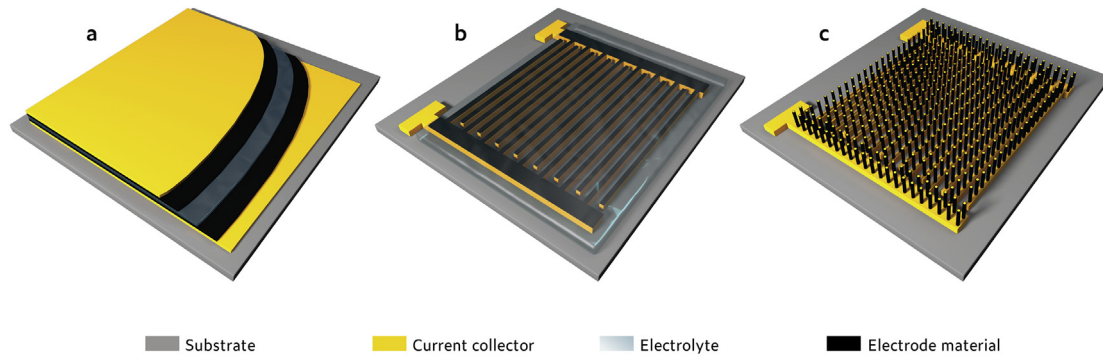


Fig. 2. Schematic showing three main configurations of microsupercapacitors. (a) Stacked configuration. (b) Interdigital finger electrode architecture. (c) 3D planar configuration.

methods between these two are quite similar. Energy (Joule, J) stored in a MSC device is physically defined as:

$$E = \int_{t_1}^{t_2} i(t)V(t)dt \quad (1)$$

Where $i(t)$ is current (Ampere, A), $V(t)$ is voltage (Volt, V), t_2 and t_1 are the bounds of the time range (Second, s). In the case of cyclic voltammetry, the time domain signal can be converted to the voltage domain with the equation:

$$V(t) = V_0 + \nu t \quad (2)$$

Where V_0 is the initial voltage in the positive scan and ν is the scan rate (V/s). Thus equation (1) can be solved as:

$$E = \frac{\int_{V_1}^{V_2} i(V)VdV}{\nu} \quad (3)$$

Where V_2 and V_1 are the corresponding lower and higher cut-off voltages. While in the case of galvanostatic charge-discharge (GCD) curves, equation (1) is solved as:

$$E = i \int_{t_1}^{t_2} V(t)dt \quad (4)$$

Equation (4) can be easily calculated by the integration of the discharge curve. And an averaged power (Watt, W) of the device can be estimated by:

$$P = \frac{E}{t_2 - t_1} \quad (5)$$

It should be noted that these equations can be obtained without distinguishing the charge storage mechanisms (independent of the capacitance or capacity), and they are widely used in the Ragone plot (after being converted to Wh and normalized to mass, area or volume of the active materials) to be compared with different energy technologies.

To distinguish the charge-storage ability of the capacitive electrode in a given potential range, capacitance is another widely used parameter to assess the performance of the electrode materials. There are good reviews discussing the difference between battery, capacitor and pseudocapacitors, as well as the correct reporting methods [51–54]. It has been demonstrated that MXene exhibits typical pseudocapacitive behaviors in a variety of electrolytes with prominent redox peaks in CV and non-linear GCD curves. The pseudocapacitance originates from the protonation of oxygen functional groups accompanied by titanium oxidation state [55]. Here we emphasize the origin of different calculation methods by briefly deriving the equations to calculate pseudocapacitance from the viewpoint of math. The capacitance C (Farad, F) is defined as the change of charge in the system to the corresponding change of potential:

$$C(V) = \frac{i(V)dt}{dV} \quad (6)$$

For CV measurements, dV/dt is defined as a constant scan rate ν . Thus, capacitance is expressed in the voltage domain:

$$C(V) = \frac{i(V)}{\nu} \quad (7)$$

Then the averaged capacitance in a given potential range can be calculated as:

$$\bar{C} = \frac{\int_{V_1}^{V_2} C(V)dV}{\int_{V_1}^{V_2} dV} = \frac{\int_{V_1}^{V_2} \frac{i(V)}{\nu} dV}{V_2 - V_1} = \frac{\int_{V_1}^{V_2} i(V)dV}{\nu^*(V_2 - V_1)} \quad (8)$$

It can thus be easily obtained by integration of the charge/discharge part of the CV curve. It has been shown that equation ($E = 1/2 \bar{C}V^2$) which is valid for dielectric/electrolytic capacitors or electrical double-layer capacitors (EDLCs) is no longer strictly hold in the case of pseudocapacitors. For GCD measurement, the averaged capacitance can only be obtained by numerical solution:

$$C = \frac{\sum_{k=1}^n \frac{i(t_{k+1} - t_k)}{V_{k+1} - V_k}}{E} \quad (9)$$

Where V_k and t_k are the voltage and time collected from GCD measurement, while E is the whole potential range. To simplify the calculation method, Béguin also suggested extracting the system capacitance by using the energy-capacitance relation [56].

$$C = \frac{2E}{V^2} \quad (10)$$

Where E is given by equation (4). Since Equation (10) also includes the influence of non-linear behavior of the discharge curve, the result is considered to be more realistic than one obtained by simple linear assumption:

$$C = \frac{i\Delta t}{\Delta V} \quad (11)$$

There is a good review recently that emphasizes the correct data reporting methods in the field [57], and these characterization standards should also be applied in the field of microsupercapacitors. Most reported publications in the field of MSCs present data directly from the final device (two-electrode measurements). This approach makes the classification of the materials (capacitive, pseudocapacitive, or battery type) even more complicated from CV and GCD measurements. Because sometimes the redox peaks are not evident in the case of two-electrode configuration, as none of the electrode potentials are fixed when current flows between the two electrodes. Thus, it is always advised to perform three-electrode tests first to distinguish the class of the material and to determine the stable electrochemical potential window of the

electrodes. This methodology should be applied for asymmetric MSC and even symmetric MSC because cations and anions do have different capacities for positive and negative electrodes. For MSCs, one should always remember that the device is a two-electrode cell, thus operating the cell below 0 V is of no practical meaning because the energy storage system is extracting energy from electronic devices rather than supplying to the system.

3. MXene for electrochemical capacitors

3.1. Synthesis approaches

Wet etching method is the most widely used method to fabricate MXenes by selectively etching one or several atomic layers from MAX phases (Fig. 3a). MAX phase compounds are ternary transitional metal carbides/nitrides ($P6_3/mmc$ symmetry) bounded by “A” element layers (usually group 13 or 14 elements such as Al or Si), where M atoms are closely packed, and X atoms occupy the octahedral sites. There are more than 70 different MAX phases discovered so far [43], including pure MAX phases, solid solutions, and ordered double transition metal structures, and there are more than 20 different MXenes that have been experimentally synthesized (Fig. 3b) [58]. Due to the difference of bond strength between M-A and M-X, “A” layers can be selectively etched with proper etchant and temperature, without disrupting the 2D layered structure of $M_{n+1}X_n$. Most MAX phases can be etched by hydrofluoric acid (HF) at room temperature, while fluoride-contained acid [59] and fluoride salt in acid [60] are also reported to be effective etchants for Ti_3AlC_2 at room temperature. To avoid direct and indirect use of HF, different synthesis routes have also been developed. For instance, molten fluoride salt can etch Al from Ti_4AlN_3 at a high temperature of 550 °C in the protection of the argon atmosphere. Hydrothermal synthesis of Ti_3C_2 is

also reported with low-toxic etchants such as NaOH [61] and $NaBF_4$ [62], and the hydrothermal process can be further extended to synthesis Nb_2C . Similar to A-site etching, the “A” site in various MAX phases (Ti_3AlC_2 , Ti_2AlC , Ti_2ZnN , and V_2AlC) can be replaced with Zn^{2+} in molten $ZnCl_2$ at high temperature (550 °C), and corresponding Cl-terminated MXenes were synthesized when employing excess $ZnCl_2$ [63]. Chemical etching process is inherently an electrochemical process driven by electron flow and Gibbs free energy; thus, electrochemical etching is ideally possible if a proper system is chosen and voltage/current are provided to the materials correctly. At room temperature, synthesis of MXene by fluoride-free electrochemical etching methods have reported. For example, Al can be electrochemically etched from both Ti_2AlC and Ti_3AlC_2 in dilute hydrochloric acid [64] and $NH_4Cl/TMAOH$ [65], respectively. But electrochemical etching can also over-etch the MAX phases to carbon. To enable a successful transition from MAX to MXene in the electrochemical etching process, the fundamental gap between etching parameters and atomic/molecular level chemical processes that govern the final products should be fulfilled.

After etching, loosely packed multilayer MXene particles (accordion-like) are obtained, which can be further converted to few-layer MXene flakes after delamination. The delamination process involves intercalation of organic molecules (urea, dimethyl sulfoxide (DMSO) [66], TBAOH [67], etc.) or metal ions [68,69], followed by sonication or gentle handshaking [70]. Those flakes form stable colloidal suspension without any surfactants due to their negatively charged surfaces. The surface terminations are usually $-OH$, $-F$ or $-O$, and aberration-corrected scanning transmission electron microscope (STEM) revealed that those functional groups prefer to stay on the top sites of the Centro-Ti atoms of the Ti_3C_2 monolayer [71]. It should be noted that when minimally intensive layer delamination (MILD) is chosen as the etching protocol, delamination happens naturally during the washing process without any

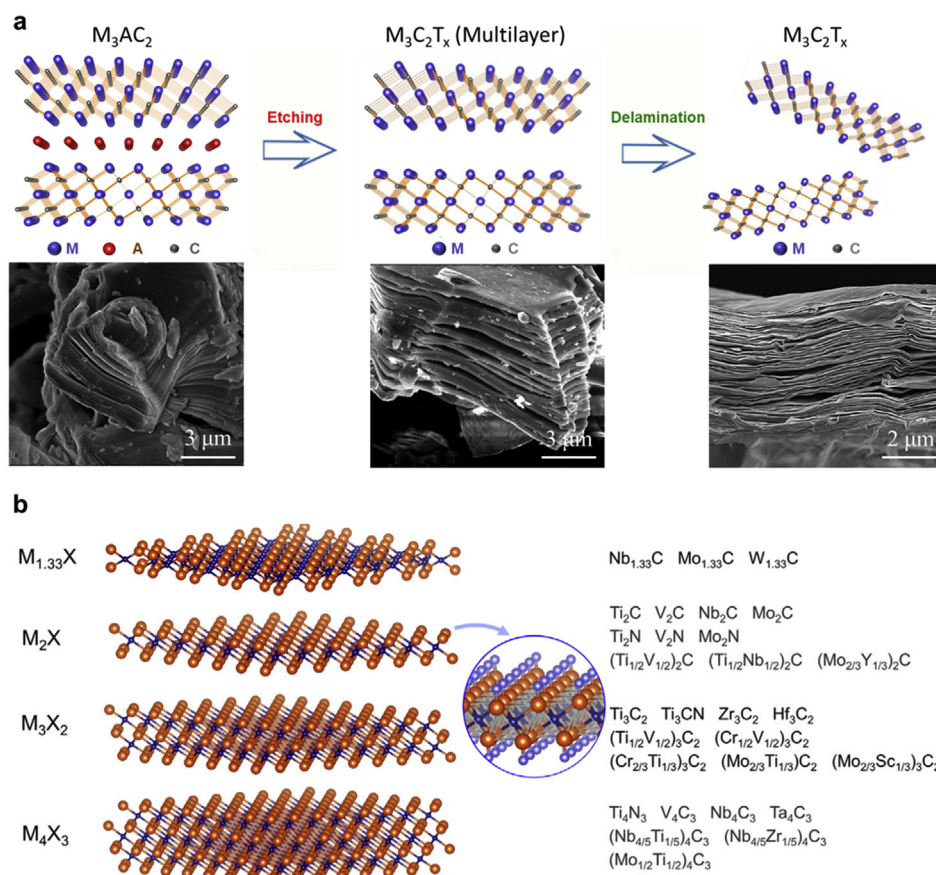


Fig. 3. (a) Schematic illustration of the synthesis process of MXenes. Multilayer MXene powder is usually fabricated by selectively removing the “A” element from MAX phase through etchants such as HF, bifluoride-based etchants (NH_4HF_2), or HF-containing fluoride-based salt ($LiF + HCl$). Delamination happens when intercalants such as DMSO, TBAOH, TMAOH, Lithium ions, and so on are introduced into the interspace of 2D sheets, after sonication (MILD method not required), stable suspensions of negatively charged delaminated 2D MXene flakes can be obtained. Reprinted with permission from Ref. [72]. Copyright 2018 Wiley. (b) MXenes obtained experimentally so far. Reprinted with permission from Ref. [58]. Copyright 2019 Cell Press.

other post-treatments [70]. The MILD method produces larger flakes of MXene with better conductivity because there is no sonication, and no insulating organic polymers are involved.

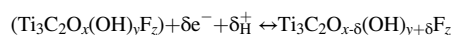
Most pure MXenes are predicted to be metallic, including Ta_3C_2 , Ta_4C_3 , Ti_3C_2 , Ti_4C_3 , Hf_2C [73], and various M_2C ($\text{M} = \text{Sc}, \text{Ti}, \text{V}, \text{Cr}, \text{Zr}, \text{Nb}, \text{Ta}$) and M_2N ($\text{M} = \text{Ti}, \text{Cr}, \text{Zr}$) MXene systems [74,75]. Manipulating the transitional metal layer or adding the functional groups have significant impacts on the electronic properties of the compounds. For example, replacing titanium with molybdenum in outer transitional layer of M_3C_2 and M_4C_3 results in the transition from metallic to semi-conducting behavior [76]. The impact of surface terminations on the electronic properties of MXenes has also been examined mostly by DFT (density functional theory)-PBE(Perdew–Burke–Ernzerhof) method, it was shown that all M_2C and M_2N MXenes become semi-conducting after the functionalization with $-\text{F}$, $-\text{O}$ and $-\text{OH}$. This is because of the hybridization of p orbitals in F or O and d orbitals in M [77]. Other theoretical studies have focused on the impact of surface terminations on specific MXenes. For example, bare Ti_3C_2 monolayer is calculated to be metallic with substantial electron states crossing the Fermi level, when $-\text{F}$ and $-\text{OH}$ terminations are introduced into the structure, $\text{Ti}_3\text{C}_2\text{T}_x$ becomes narrow bandgap semi-conductors or metals, depending not only on the type of terminations, but also their arrangement. For instance, when F atoms locate above the hollow sites between the neighboring C atoms, it exhibits a narrow bandgap of 0.04 eV; When F atoms locate above topmost C atoms, it is metallic [40,78]. DFT calculation has also shown the metallic behavior of $\text{Ti}_3\text{C}_2\text{S}_2$ monolayer [79]. In contrast, many other O-terminated MXenes are also predicted to be semi-conducting: Sc_2CF_2 has a indirect bandgap of 1.03 eV; $\text{Sc}_2\text{C}(\text{OH})_2$ has a direct band of 0.45 eV; Zr_2CO_2 has a indirect bandgap of 0.88 eV and Hf_2CO_2 has an indirect bandgap of 1 eV [74]. Experimentally, increased electronic conductivity of MXenes has been observed after surface de-functionalization of $-\text{F}$ and $-\text{O}$ groups. After vacuum annealing, 4, 6, >10, and 6 times increase in the conductivity have been measured in the multi-layer MXenes samples, including $\text{Ti}_3\text{C}_2\text{T}_x$, Ti_3CNT_x , and $\text{Mo}_2\text{TiC}_2\text{T}_x$ [38].

3.2. MXene in aqueous electrolyte

Various cations such as Li^+ , Na^+ , K^+ , NH_4^+ , Mg^{2+} , Al^{3+} can be intercalated electrochemically between MXene layers [80]; thus, MXenes are promising candidate electrode materials for electrochemical capacitor and mono- or multivalent ion batteries. Unlike EDLC that store charges by the physical absorption of electrolyte ions onto the electrode surfaces, MXene electrodes offer high volumetric capacitance at high charge and discharge rates, which is from fast surface redox reactions (known as

pseudocapacitance), high electronic conductivity and high density of the electrode. A summary of the electrochemical performance of MXenes synthesized from different etching and delamination conditions is shown in Table 1.

$\text{Ti}_3\text{C}_2\text{T}_x$ is the most studied MXene so far for electrochemical capacitors. Intercalation of some cations happens spontaneously when MXene samples are exposed to the electrolyte; further, in-situ XRD demonstrated that the interlayer spacing changes during the cycling process of $\text{Ti}_3\text{C}_2\text{T}_x$ in Li^+ , Na^+ , K^+ , NH_4^+ , Mg^{2+} , or Al^{3+} containing electrolyte, indicating the ion and H_2O intercalation during the charge/discharge process [80]. In addition, in situ X-ray absorption near edge structure spectroscopy (XANES) further confirmed the continuous Ti oxidation state change during cycling [96]. On the other side, $\text{Ti}_3\text{C}_2\text{T}_x$ shows low specific surface area, thus electrostatic double-layer capacitance should be low; these behaviors clearly indicate the pseudocapacitive nature of $\text{Ti}_3\text{C}_2\text{T}_x$. In particular, it shows remarkable pseudocapacitance in acid media as compared with electrolytes containing other ions. The typical charge storage mechanism of $\text{Ti}_3\text{C}_2\text{T}_x$ in the acid media is given as [96].



In-situ Raman reveals that the hydronium in the acid electrolyte is involved in the bonding with oxygen termination on the surface of $\text{Ti}_3\text{C}_2\text{T}_x$, and this process changes the oxidation state of titanium [55]. Moreover, Dall'Agnese et al. demonstrated that the oxygen-containing terminations could also replace fluorine functional groups by artificially designed intercalation of potassium salts [84]. Electrochemical properties of the as-synthesized MXene flakes are not only influenced by the surface terminations of MXene flakes, but also the flake size and defects. Maleski et al. tested the electrochemical performance of $\text{Ti}_3\text{C}_2\text{T}_x$ with different sizes ranging from 0.1 to 5 μm [97], MXene flakes with a lateral dimension of 1 μm showed best gravimetric capacitance while flakes with a lateral dimension of 0.35 μm showed the best capacitance retention when scan rate increases. Smaller flakes are supposed to have better accessibility with electrolyte, but they also show decreased electronic conductivity, optimized electrochemical properties for specific applications may need a balance between that trade-off. As electrode materials for electrochemical capacitors, $\text{Ti}_3\text{C}_2\text{T}_x$ MXene is found to undergo irreversible oxidation in the aqueous electrolyte in the positive potential window, mainly from the oxidation of Titanium atoms in the defect sites [98]. However, the anodization process at certain degrees does not oxidize MXene completely but instead stabilized the surface of the flakes by introducing the oxidation debris (Fig. 4a–e). Raman spectrum shows strengthened peaks that are assigned to out-of-plane vibrations of C atoms in $\text{Ti}_3\text{C}_2\text{O}_2$ (631.4 and 725 cm^{-1}), meaning

Table 1

Summary of electrochemical performance of various MXenes (All from three-electrode measurement).

Material	Precursor	Etchant	Temperature (°C)	Delamination	Electrochemical test	Performance	
						(F/cm ²)	(F/g)
$\text{Ti}_3\text{C}_2\text{T}_x$	Ti_3AlC_2	9 M HCl+7.5 M LiF [81]	35 (24 h)	sonication	$\text{Ti}_3\text{C}_2\text{T}_x/\text{rGO}$ film	N/A	254 (2 mV/s)
		50% HF [80]	RT (18 h)	DMSO	$\text{Ti}_3\text{C}_2\text{T}_x$ paper	442	130 (2 mV/s)
		6 M HCl + 5 M LiF [60]	40 (45 h)	N/A	Clay	900	245 (2 mV/s)
		9 M HCl+49% HF [82]	N/A (24 h)	LiCl	$\text{Ti}_3\text{C}_2\text{T}_x/\text{PAN-carbon fiber}$	N/A	88 (10 mV/s)
		50% HF [45]	RT (18 h)	DMSO	$\text{Ti}_3\text{C}_2\text{T}_x/\text{PVA-KOH}$	~530	~170 (2 mV/s)
		9 M HCl+3.8 M LiF [83]	35 (24 h)	sonication	$\text{Ti}_3\text{C}_2\text{T}_x/\text{rGO}$ film	1040	335.4 (2 mV/s)
		N/A [84]	N/A	DMSO	$\text{Ti}_3\text{C}_2\text{T}_x$ film	520	325 (2 mV/s)
		9 M HCl+1.9 M LiF [85]	35 (24 h)	sonication	$\text{Ti}_3\text{C}_2\text{T}_x/\text{CNT}$ yarn	1083	532 (2 mA/cm ²)
		9 M HCl+3.8 M LiF [86]	35 (24 h)	sonication	$\text{Ti}_3\text{C}_2\text{T}_x/\text{AC}$ film	38	126 (10 mV/s)
		9 M HCl+3.8 M LiF [87]	35 (24 h)	Sonication	$\text{Ti}_3\text{C}_2\text{T}_x/\text{PPy}$ film	1000	416 (5 mV/s)
		12 M HCl+3 M LiF [88]	35 (48 h)	Not required	$\text{Ti}_3\text{C}_2\text{T}_x/\text{SCNT}$ film	314	N/A
		2.25 M NH_4F [89]	150 (24 h)	No (powder)	$\text{Ti}_3\text{C}_2\text{T}_x$ + Carbon black + PVDF	141	N/A
		6 M HCl + LiF [90]	50 (48 h)	No (powder)	$\text{Ti}_3\text{C}_2\text{T}_x/\text{rGO}$ + Carbon black + PVDF	N/A	154.3 (2 A/g)
		10% HF [91]	RT (10 h)	No (powder)	Ti_3CT_x + Carbon black + PTFE	N/A	51 (1 A/g)
Ti_2CT_x	Ti_2AlC	48% HF [92]	RT (10 h)	TBAOH	$\text{Mo}_{1.33}\text{C}$ Paper	1100	339
$\text{Mo}_{1.33}\text{C}$	$(\text{Mo}_{2/3}\text{Sc}_{1/3})_2\text{AlC}$	14 M HF [93]	55 (160 h)	TBAOH	Mo_2CT_x paper	700	200 (2 mV/s)
Mo_2CT_x	$\text{Mo}_2\text{Ga}_2\text{C}$	28 M HF [94]	RT (45 h)	TBAOH	clay	N/A	487 (2 mV/s)
V_2C	V_2AlC	50% HF [95]	55 (48 h)	isopropylamine	$\text{Nb}_2\text{CT}_x/\text{CNT}$ film	325	165 (5 mV/s)
Nb_2CT_x	Nb_2AlC						

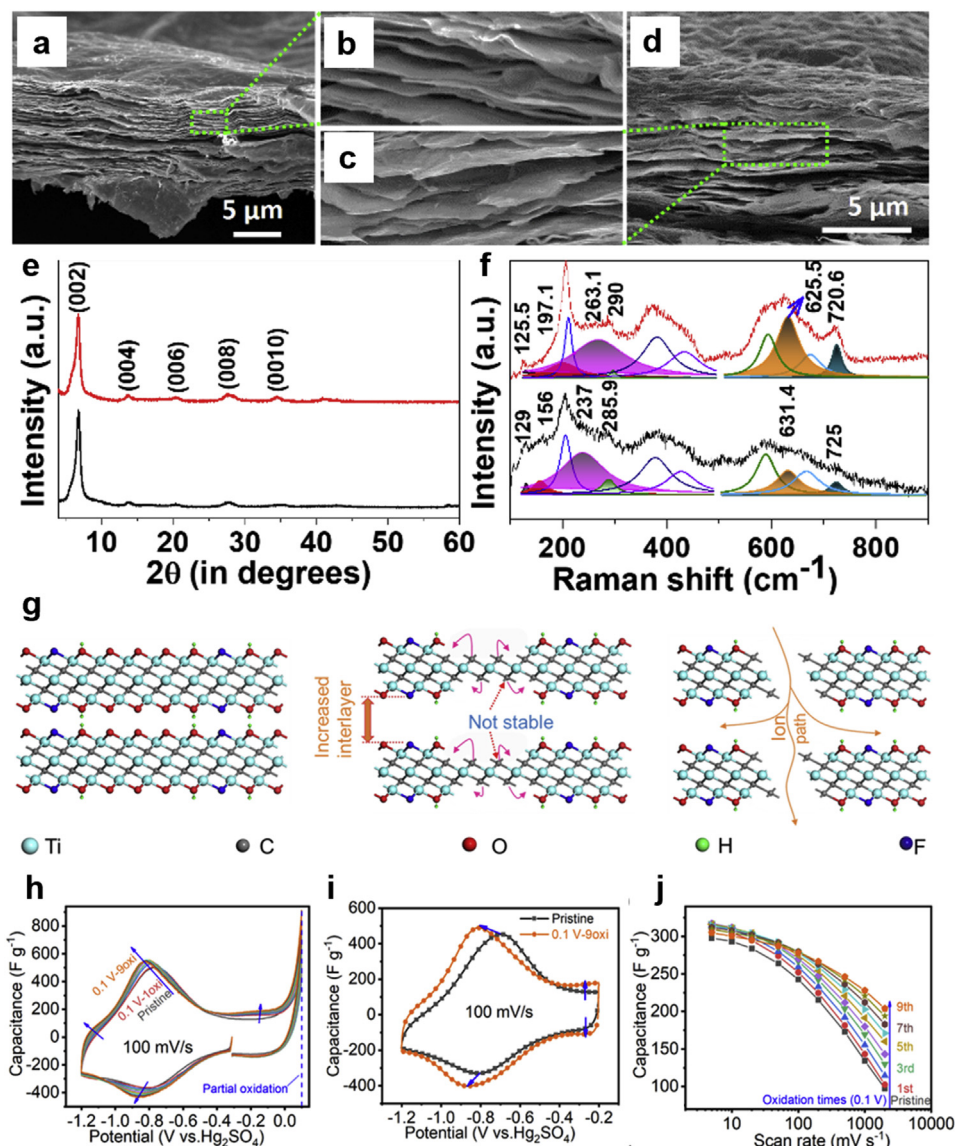


Fig. 4. SEM images showing MXene free-standing film (a) before and (d) after anodic scan; (b) and (c) show the corresponding high-resolution cross-section images, (e) X-ray diffractogram and (f) Raman spectra of $\text{Ti}_3\text{C}_2\text{T}_x$ MXene film electrode before (black plot) and after (red plot) anodization. Reprinted with permission from Ref. [98]. Copyright 2018 Royal Society of Chemistry. (g) Schematic showing the oxidation process in the over oxidation scan of (h). (i) CV scan of $\text{Ti}_3\text{C}_2\text{T}_x$ before and after partial oxidation. (j) Capacitance versus scan rates for MXenes after different cycles of anodic scans. Reprinted with permission from Ref. [99]. Copyright 2019 Wiley. (For interpretation of the references to colour in this figure legend, the reader is referred to the Web version of this article.)

oxygen-containing functional groups are introduced after the anodic scan (Fig. 4f). As we mentioned before, oxygen termination on the surface of $\text{Ti}_3\text{C}_2\text{T}_x$ bond/debonded with hydronium ions during charging and discharging in the acid media, thus improved pseudocapacitance may be obtained by properly control the oxidation process. Indeed, Tang et al. demonstrated that controlled anodic oxidation can also increase the interlayer space of $\text{Ti}_3\text{C}_2\text{T}_x$ and creates pores in the 2D nanosheets (Fig. 4g) [99]. The oxidation process (Fig. 4h) opens more active sites and improve the ion diffusion in the electrode material, resulting in improved capacitance (Fig. 4i) and rate performance (Fig. 4j) at high scan rates.

3.3. Non-aqueous electrolytes for MXene

$\text{Ti}_3\text{C}_2\text{T}_x$ MXene in the aqueous electrolyte has a limited potential window (−1.1 to −0.1 V versus $\text{Hg}/\text{Hg}_2\text{SO}_4$, on glassy carbon electrode) [46]. In order to increase their energy density, an organic-based (potential window of 2.5–2.7 V) and ionic-liquid- electrolytes (potential window of 3.5–4 V) need to be developed to increase the operation potential window of MXene electrodes, and the cell voltage of MSCs ($E = 1/2CV^2$). Only several reports have been published on the electrochemical performance of MXene electrodes in non-aqueous electrolytes [45,100–103], and an understanding of the interactions between MXene

electrode and such electrolytes is lacking. In general, an ideal electrolyte should have a wide potential window, high ionic conductivity, strong chemical inertness to the electrode materials, excellent thermal stability, and matching of the electrolyte ion sizes with the pore structure of the electrode materials. To explore the possibility, Satoshi demonstrated that the steric chloride termination in the Ti_2CT_x electrode could open the interspace and increase the accessibility of Li^+ in ethylene carbonate(EC)-diethyl carbonate electrolyte (DEC) [103]. As a result, high volumetric ($130 \text{ F}/\text{cm}^3$) and gravimetric capacitance ($300 \text{ F}/\text{g}$) were achieved. Further, Wang et al. examined the electrochemical performance of $\text{Ti}_3\text{C}_2\text{T}_x$ in a variety of Li^+ containing electrolytes such as propylene carbonate (PC), acetonitrile (ACN), and dimethyl sulfoxides (DMSO) [102]. Although ACN has the highest ionic conductivity, MXene in PC showed the highest discharge gravimetric capacitance ($195 \text{ F}/\text{g}$) and coulombic efficiency (96%) (Fig. 5a). The electrochemical impedance spectroscopy (EIS) analysis also indicated that $\text{Ti}_3\text{C}_2\text{T}_x$ in PC shows the minimum deviation from capacitive behavior in the low-frequency region (Fig. 5b). The superior performance of $\text{Ti}_3\text{C}_2\text{T}_x$ in PC can be explained by the desolvation process during the charging process, while in the case of DMSO and ACN, Li^+ is pulling the solvent molecules into the interspace of $\text{Ti}_3\text{C}_2\text{T}_x$ during charging (Fig. 5c).

Ionic liquids are another class of promising electrolytes because of

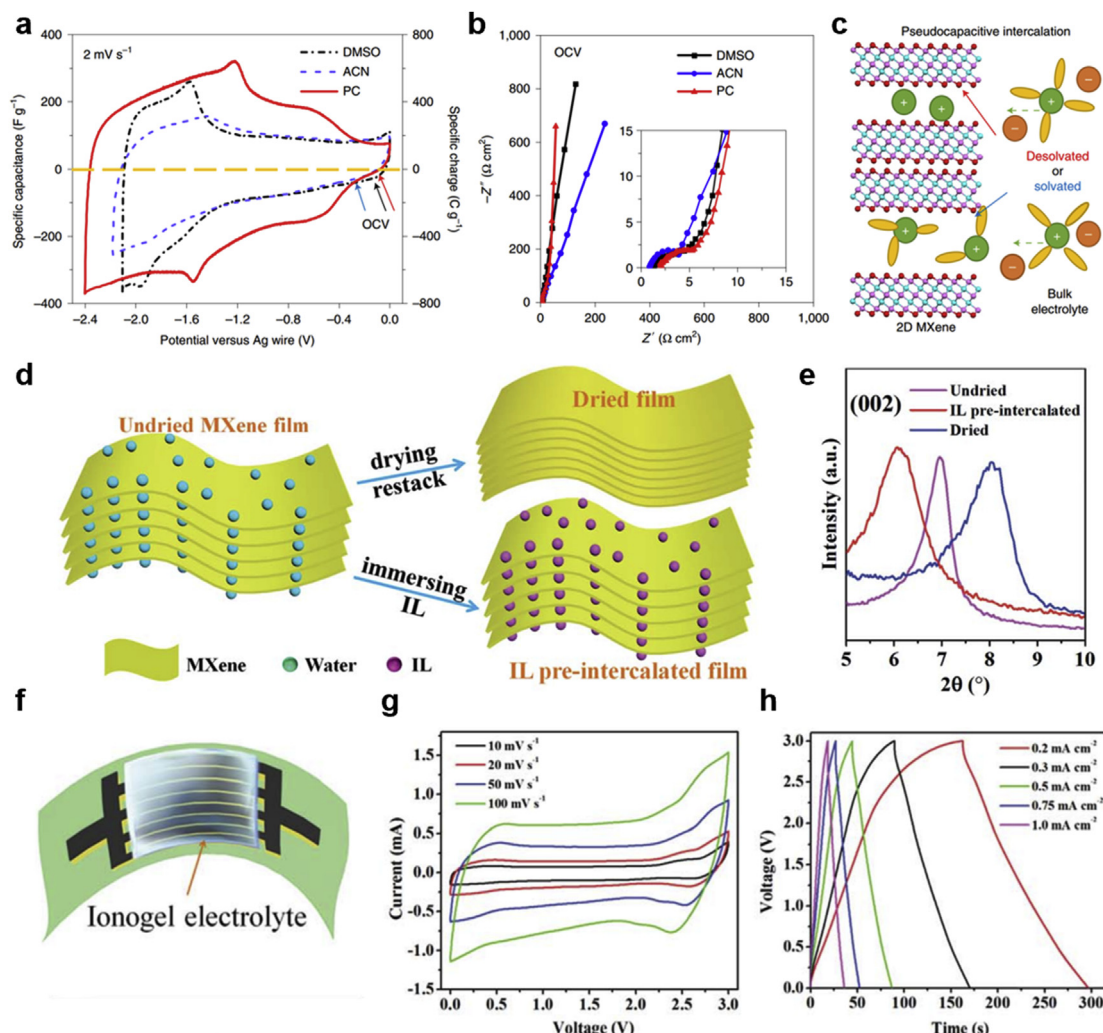


Fig. 5. (a) CV curves and (b) EIS measurement of macroporous $\text{Ti}_3\text{C}_2\text{T}_x$ electrode with 1 M LiTFSI in DMSO, ACN, and PC electrolytes. (c) Schematic showing the charging process with different organic electrolytes. Reprinted with permission from Ref. [102]. Copyright 2019 Springer Nature. (d) Schematic illustration of the pre-intercalation process of $\text{Ti}_3\text{C}_2\text{T}_x$ with ionic electrolyte. (e) XRD patterns among the film prepared by different methods. (f) Schematic of the all-solid-state MXene MSC with ionogel. (g) CV curves and (h) GCD profiles for the all-solid-state MXene MSC. Reprinted with permission from Ref. [105]. Copyright 2019 Royal Society of Chemistry.

their wide operation potential window and high thermal and chemical stability, as they are liquid salts composed of solely ions with melting points below 100°C . As-prepared $\text{Ti}_3\text{C}_2\text{T}_x$ clay exhibits a low capacitance of 32 F/g in 1-Ethyl-3-methylimidazolium bis(trifluoromethylsulfonyl) imide (EMI-TFSI) due to the restacking problem of the $\text{Ti}_3\text{C}_2\text{T}_x$ flakes, the accessibility of EMI^+ can be improved by delamination and adding carbon nanotubes, and capacitance up to 85 F/g has been achieved [104]. Further, Lin et al. immersed the $\text{Ti}_3\text{C}_2\text{T}_x$ hydrogel in EMI-TFSI to prevent the restacking problem, and the resulting ionogel film shows a capacitance of 70 F/g in a large potential window of 3 V . To fabricate high-voltage MXene based MSCs, Zheng et al. developed ionogel based MXene MSCs with the ionic liquid pre-intercalated MXene film [105]. After immersing $\text{Ti}_3\text{C}_2\text{T}_x$ in the ionic liquid, an enlarged interlayer spacing is observed as expected (Fig. 5d–e). This pre-intercalated $\text{Ti}_3\text{C}_2\text{T}_x$ can be patterned into interdigital electrodes by shadow mask-assisted vacuum filtration process. After applying EMIMBF₄/PVDF-HFP ionogel electrolyte, an as-fabricated ionogel-based MXene device shows excellent flexibility and high volumetric capacitance (133 F/cm^3). (Fig. 5f–h).

4. Fabrication methods for MXene Microsupercapacitor

So far, various techniques have been reported to realize MSC patterns

in the submillimeter scale. For the planar type configuration, the challenges originate mainly from the following factors: 1) sufficient resolution of the patterns defined by patterning methods; 2) compatibility with the conditions employed in the semiconductor industry (such as the vacuum deposition procedures) to enable co-integration with other electronic components; 3) depositing the active electrode materials effectively onto the microsized current collector patterns without shorting the positive and negative electrodes.

In this section, different patterning techniques for MXene-based MSCs are summarized (Fig. 6), including their advantages and limitations. In general, these fabrication techniques can be categorized into two categories: 1. Direct patterning of MXene solid on the desired substrate by techniques such as laser scribing or reactive ion etching. 2. Transferring the MXene ink into different patterns by various printing techniques. We summarize and evaluate the recent developments in these techniques as well as the final performance of the devices next.

4.1. Photolithography

Photolithography is a cost-effective and straightforward micro-fabrication method that defines and transfer high-resolution patterns onto various substrates. It has been widely used for the fabrication of

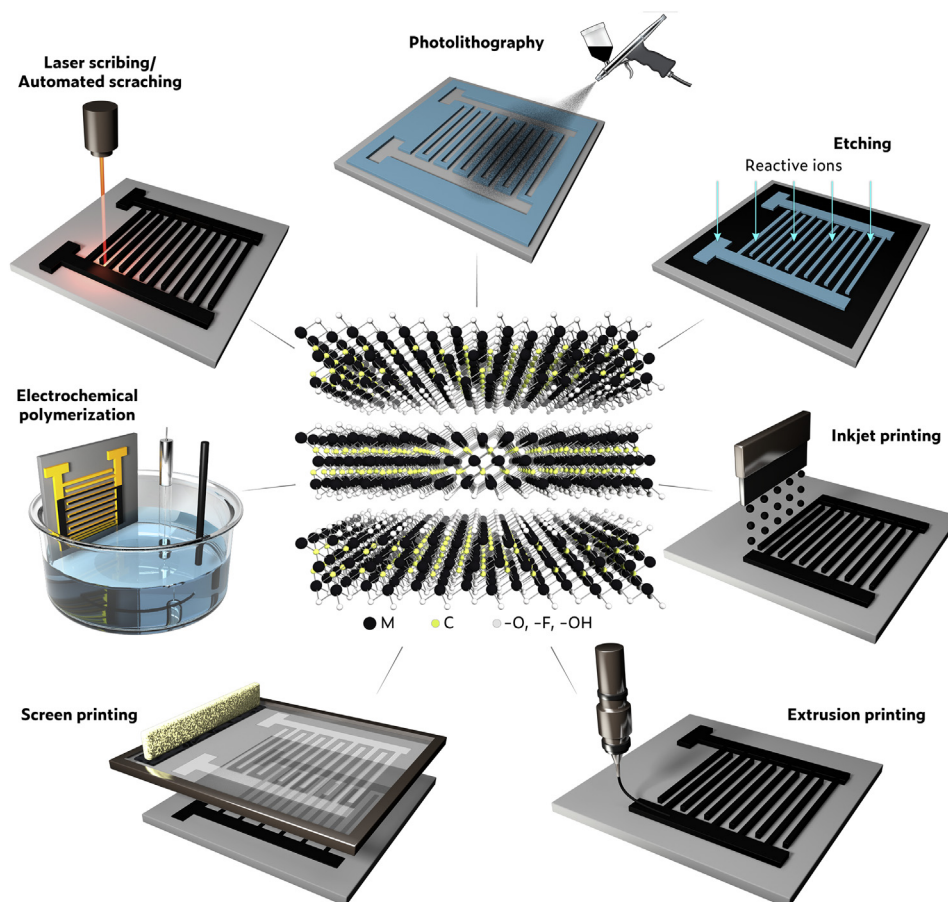


Fig. 6. Different Fabrication methods for interdigital MXene microsupercapacitors.

microelectromechanical systems (MEMS), complementary metal-oxide-semiconductor (CMOS) devices, and integrated circuits. Via the exposure of light through a photomask, the photosensitive photoresist can be patterned to any shape as designed, making it useful for the fabrication of MXene microsupercapacitors. For example, after an oxygen plasma treatment on the surface of the gold current collector, Jiang et al. showed that MXene dispersions could be easily sprayed onto the pre-defined current collector and get firmly attached to the current collector (Fig. 7a) [106]. The lift-off process in the photolithography process usually involves bath sonication in an organic solvent such as acetone; it was shown that the adhesion of MXene flakes and the gold current collectors are firm that no peeling was observed after sonication (Fig. 7b–c). As a result, the device showed an ultra-high scan rate capability up to 300 V/s (Fig. 7d) and a very short resistor-capacitor (RC) time constant of 1.1 ms (Fig. 7e). Photolithography has not been widely used in the fabrication of MXene microsupercapacitors because limited electrode materials can be deposited onto the current collector, resulting in insufficient energy density. The areal capacitance of MXene microsupercapacitor can be improved by creating deep cavities of the interdigital geometry; for instance, Xu et al. built 300 μm SU-8 photoresist between the pre-patterned interdigital Cr/Au current collectors [107], the high-aspect-ratio structure of the photoresist can accommodate higher mass loading of the active materials. After injecting the $\text{Ti}_3\text{C}_2\text{T}_x/\text{PE}$ suspension and solidifying the electrode, the final device showed a high areal capacitance of 276 mF cm^{-2} and capacitance retention of 95% after 1000 cycles. The deep cavities take advantage of the thick electrode materials, but since no 3D effect is highlighted [108], poor rate performance was observed as the device with thick electrode showed a high resistance of 40 Ω and areal capacitance drops 25% when scan rates increased from 20 mV/s to 100 mV/s .

MXene can also be selectively deposited onto the pre-patterned current collector by electrophoretic deposition. During the electrophoretic deposition (EPD), charged particles in the suspension move toward the electrode with opposite polarity and then coagulate on it. Xu et al. first reported the electrophoretic deposition of MXene in acetone solvent [109], the H^+ ions in the solution is claimed to be absorbed on the surface of MXene flakes and help stabilize the colloid. Since MXene flakes with absorbed H^+ have positive surface charges, they move towards the cathode during the electrophoretic deposition, and a uniform layer-by-layer deposition observed when Nickel foam was used as both cathode and anode. Collini et al. further extended the electrophoretic deposition of MXene in aqueous and other organic solvents [110]. Interestingly, in contrast to Xu's paper, since delaminated MXene flakes have a negative charge and form stable aqueous suspension itself, they can directly be deposited on the anode FTO substrate even when a moderate potential of 5 V was applied to the cathode and anode. Later on, robust $\text{Ti}_3\text{C}_2\text{T}_x/\text{CNT}$ films were also prepared by a simple yet effective EPD method [111]. Since electrophoretic deposition has been demonstrated to be a robust method to deposit MXene on the substrate, it is worth to explore this method for the fabrication of MXene microsupercapacitor as no literature has been reported for this direction. Qin et al. reported another simple strategy to fabricate MXene microsupercapacitor, they fabricated MXene-polymer composite by electropolymerization of the MXene/monomer suspension and showed MXene flakes could be self-assembled to positively charged conductive polymer chains as counter ions dopant and form molecular-level contact [112]. As a result, the composite of MXene and conducting polymers shows an interconnected porous structure, and the prototype MSC showed an areal capacitance of 47.4 mF cm^{-2} and a high energy capability of 20.05 mWh cm^{-3} .

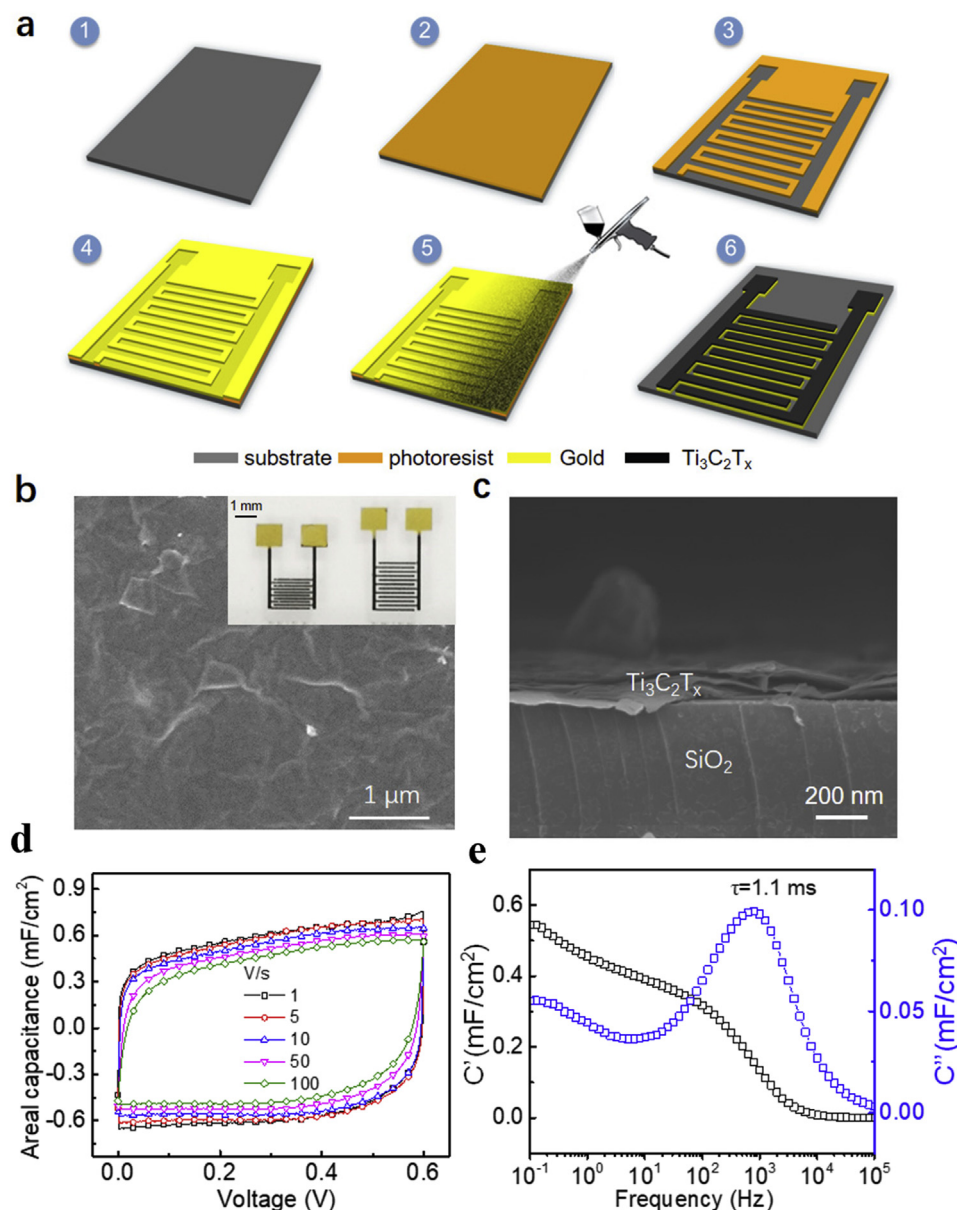


Fig. 7. (a) Schematic illustration of the fabrication process of MXene microsupercapacitors by photolithography and spray coating. (b) Top-view and (c) cross-sectional SEM images of Ti₃C₂T_x layer on gold, inset in (b) shows the digital photos of the MXene microsupercapacitor device. (d) CV curves of Ti₃C₂T_x micro-supercapacitor (thickness of 0.3 μm) measured at different scan rates. (e) C' and C'' versus frequency for Ti₃C₂T_x microsupercapacitor. Reprinted with permission from Ref. [106]. Copyright 2019 Wiley. (For interpretation of the references to colour in this figure legend, the reader is referred to the Web version of this article.)

4.2. Laser engraving

The laser scribing technique is a cost-effective and straightforward method to create customized patterns on various substrates in a single step. It offers excellent flexibility in terms of materials that can be ablated and the depth of the field. The difficulty of using a laser processing is to find the correct wavelength, pulse energy, and scanning speed of the laser to get a proper resolution. Laser technology has been widely used in the fabrication of MSCs either by selective reduction of GO/polyimide [22] or directly burns the active materials film to obtain desired patterns. In 2016, Peng et al. first employed laser scribing technique to make solid-state All-MXene MSC [113], a layer of large-size Ti₃C₂T_x was first spray-coated onto the substrate as current collector followed by the top layer of small-size Ti₃C₂T_x, which were then patterned by a 10.6 μm CO₂ laser. The CO₂ laser removes the MXene in the exposed region by generating a high heat flux that vaporizes the material, but since the local heat generated by the laser cannot dissipate rapidly enough through the underlying glass, the edges the patterned the interdigital fingers are not even and smooth (Fig. 8a). Similarly, Kurra et al. employed laser machining to fabricated MXene-on-paper coplanar microsupercapacitors

over a large area. It was shown that the laser could even pattern thick MXene film up to 120 μm [114], and the versatility of this technique was also shown with a similar process to pattern a thick free-standing MXene film [115]. Stretchable and twistable solid-state MSC arrays were fabricated from laser-machined specifically designed kirigami patterns.

To minimize the restacking problem of in the MXene film, three dimensional(3D) electrodes were designed by building a rGO/MXene aerogel [116], such thick and porous structure can only be patterned through a laser cutting process, and the final MSC device presented good areal capacitance of 34.6 mF cm⁻² and excellent cycling performance. Although no substrate is used in these cases, the local high temperature from the laser still cannot dissipate fast enough, and uneven structures are observed at the edge of the electrode fingers. An improvement has been made by Huang et al., they reported a laser machining process to pattern the free-standing MXene film using a cold ultraviolet laser. The advantage of this laser is that it can ablate materials without causing too much surface heating because of its short pulse duration (Fig. 8b) [117]. No unwanted edge defects are observed since a cold laser is used, and thus it is anticipated that less oxidation happens during the laser scribing process, resulting in better performance of the final MSC device. After

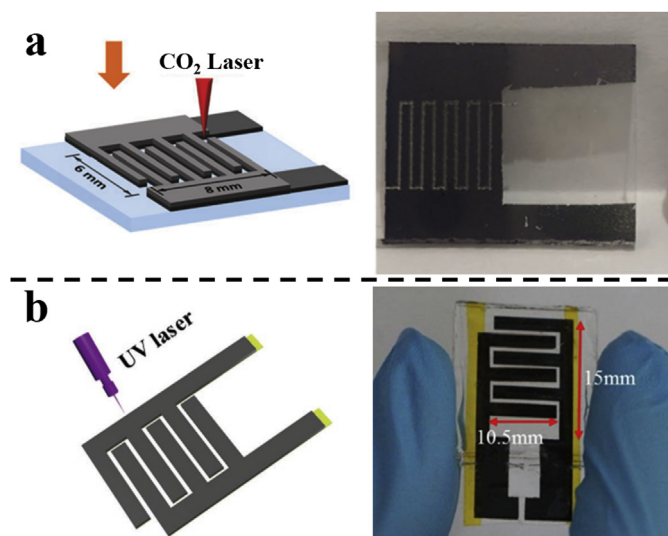


Fig. 8. Schematic illustration for the fabrication of MXene MSC using different laser scribing processes. Digital Photos show the final interdigital fingers of the laser cut MXene by (a) CO₂ laser, Reprinted with permission from Ref. [113]. Copyright 2016 Royal Society of Chemistry; and (b) UV laser, Reprinted with permission from Ref. [117]. Copyright 2018 Wiley.

applying gel electrolyte (PVA/H₂SO₄), the free-standing MXene MSC showed excellent mechanical flexibility as well as outstanding electrochemical performance (areal device capacitance up to 340 mF cm⁻²). Although cold laser has a short pulse duration, the strength of laser power is still strong enough to create microchannels in most materials. For instance, Wang et al. first used a simple slurry-coating technique to coat MXene on both sides of the Ni sheet (20 μm thick), then cold laser was used to create the microchannels in the interdigital fingers. Benefiting from the penetration depth of the laser, both sides of the current collector could be effectively utilized, which is an innovative strategy to increase

the areal energy density of the MSC device in a given footprint area.

4.3. Screen printing

Screen printing is a traditional technique that can create electrodes for mass production in a stable and reproducible manner. An ink-blocking stencil is supported by woven meshed and placed in a few millimeters above the target substrate, after loading the ink on the screen mesh, a squeegee is swept across the woven meshes and forces inks to penetrate through the open areas to the surface of the substrates. After drying, the inks can solidify and form the desired patterns. The resolution of the screen-printed designs relies on the resolution of the stencil as well as the rheological properties of the inks. The commercial state-of-art stencil can reach a minimum resolution of 5 μm [118], which is sufficient for the fabrication of microsupercapacitors as most reported MSC devices to have a feature size larger than 100 μm. Inks for screen printing usually should have high viscosity and moderate shear thinning behavior, which can be achieved by increasing the concentration of the active materials or adding some inactive additives [119]. Li et al. developed thixotropic composite ink made of hydrous ruthenium oxide [120], MXene nanosheets, and conductive silver nanowires for screen printing (Fig. 9a). By evaluating elastic modulus G' (meaning the amount of energy stored in the material under shear) and the loss modulus G'' (meaning the energy density lost under shear, mainly due to the friction and particle movement inside) as a function of oscillation strain, they found that both pure MXene ink and composite ink (MXene + RuO₂+silver nanowires (AgNWs)) exhibit solid-like behavior below their yield stress (beneficial for solidification on the substrate), but when shear stress is applied above the yield point, they both show liquid-like behavior, meaning a fluent flow of the ink through the stencil during the screen printing process. All printed patterns show high resolution and smooth edges from both optical and SEM images (Fig. 9b). It was also demonstrated that AgNWs are uniformly distributed in the composite and can effectively i) prevent the restacking problem of the MXene nanosheets; ii) increase the mechanical stability and conductivity of the composite. Similarly, Xu et al. fabricated a flexible asymmetric

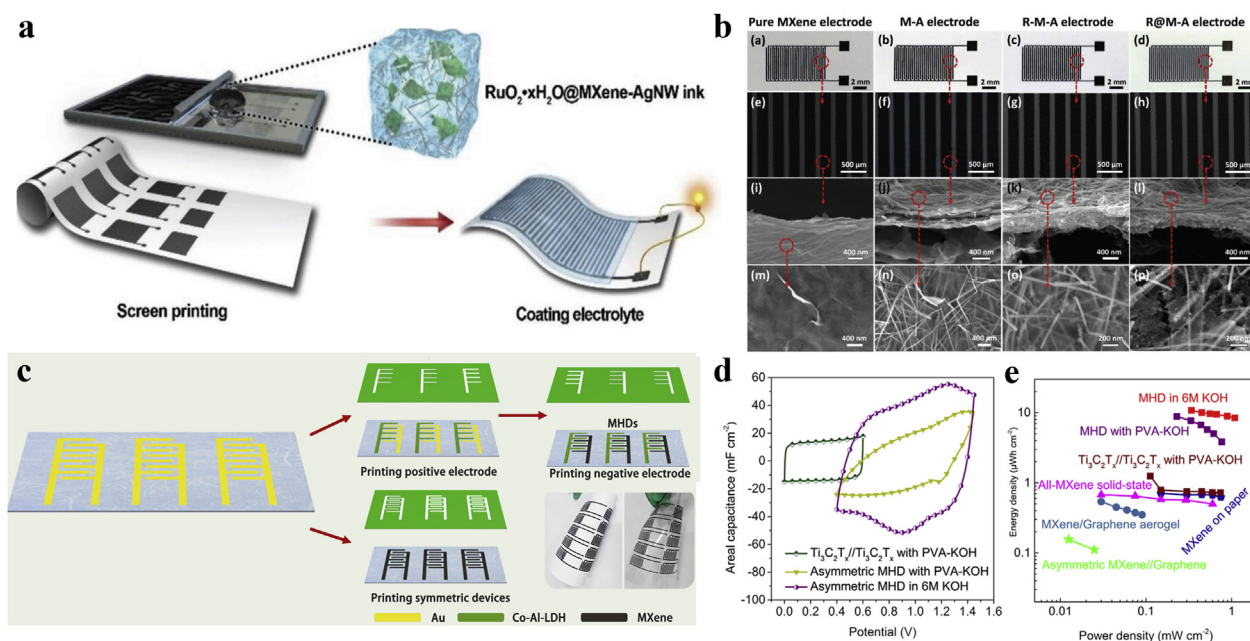


Fig. 9. (a) Schematic showing the screen printing process of MSC from RuO₂·xH₂O@MXene-AgNW ink. (b) Optical and SEM images of the printed MSCs. Reprinted with permission from Ref. [120], Copyright 2019 Wiley. (c) Asymmetrical MXene MSCs fabricated by the modified screen-printing process. (d) CV curves of asymmetric MXene MSCs with different electrolytes and symmetric device with PVA-KOH gel electrolyte at a scan rate of 30 mV/s. (e) Ragone plot comparing the performance of the asymmetric MXene MSC with other reported literature. Reprinted with permission from Ref. [121], Copyright 2018 Elsevier.

microscale hybrid device (MHD) by a two-step selective screen-printing process (Fig. 9c) [121], Co–Al-layered double hydroxides (Co–Al-LDH) electrodes was chosen as the positive electrode to match with the charge of $\text{Ti}_3\text{C}_2\text{T}_x$ in the negative side. Compared with symmetric MXene MSC, the asymmetric device offers wider voltage window as well as areal capacitance (Fig. 9d). As a result, the screen-printed asymmetric MSC exhibits a high energy density of $10.80 \mu\text{Wh cm}^{-2}$ in 6 M KOH aqueous electrolyte, which is much higher than symmetric MXene MSC ($1.25 \mu\text{Wh cm}^{-2}$) fabricated in the same protocol (Fig. 9e). The asymmetric device also remained 92% of its original capacitance after 10 k cycles long term stability test in a current density of 1.25 mA cm^{-2} .

4.4. Inkjet printing

Inkjet printing is another technology that was used to directly define the interdigital geometry out of functional MXene inks. Although the roots of this technology dates back to Lord William Kelvin in the nineteenth century, for his invention of siphon recorder that operated by applying electrostatic force to control direction of the droplets to paper [122], inkjet printing did not gain significant attention until significant advance has been made to the computer-controlled drop-on-demand graphic output and the further developments in the fields of nanomaterials and nanotechnology to reduce the cost and improve the precision of the printing process. Nowadays, inkjet printing is widely used in a wide range of applications such as thin-film transistors [123], solar cells [124], light-emitting devices [125], sensors [126] and pharmaceutical applications [127]. Inkjet printing can provide excellent precision of the printed materials on various substrates, and the printing speed is faster than screen printing, during the printing process, a small volume of inks is positioned onto the substrate before being transformed into a solid. Since the volume of inks is limited during each printing cycle, functional materials may need to be print layer by layer to meet the desired thickness. The versatility of the technique reflects the simplicity in the operation procedures. At the same time, to generate excellent and fluent droplets and produce precise patterns, there are also several physical operations that constrain inkjet printing. We first address the importance of these physical constraints and then provide a guideline for tuning the MXene ink properties for inkjet printing.

Three main constants, Reynolds (Re), Weber (We) and Ohnesorge (Oh), defines the primary behavior of the liquids:

$$Re = \frac{\rho v a}{\eta} \quad (12)$$

$$We = \frac{v^2 \rho a}{\gamma} \quad (13)$$

$$Oh = \frac{\sqrt{We}}{Re} \quad (14)$$

Where ρ is the density (kg/m^3), η , and γ is the dynamic viscosity ($\text{N}\cdot\text{s/m}^2$) and surface tension (N/m) of the liquid. v is the velocity (m/s), and a is the nozzle diameter (m). The inverse Ohnesorge number Z is commonly used to predict a proper drop formation, which is defined as $Z = 1/Oh$. Numerical simulation has shown that the rheology of the ink should be in the following range, $1 < Z < 10$, to generate stable droplets [128]. When Z is low, ink is too viscous to be ejected, while the high value of Z means lots of satellite drops accompany the primary droplet. In order to overcome the energy barriers from the fluid/air surface tension at the nozzle, Weber's number should have a minimum value of 4. After the drop ejects, there is a threshold that considered to cause splashing of the droplet, an experimental threshold to avoid splashing is given by Ref. [129]:

$$We^{\frac{1}{2}} Re^{\frac{1}{3}} > f(R)$$

Where $f(R)$ is highly depended on the roughness and surface energy of

the substrate, for smooth surface $f(R) \approx 50$, to meet all these requirements for successful inkjet printing, proper solvent and concentration of the active materials should be evaluated, while the diameter of the nozzle diameter is usually fixed by the manufacturer of the cartridges.

MXene with different thickness was reported to present different rheological characteristics when dispersed in water. Akuzum et al. systematically studied the rheological properties of single- and multi-layer $\text{Ti}_3\text{C}_2\text{T}_x$ dispersions [130]. It was found that multilayer MXene suspension can exhibit flowability even at a very high concentration of 70 wt%, making them suitable for fabrication techniques such as ink-jet printing or extrusion printing. In contrast, single-layer MXene dispersion shows elasticity even at a low concentration of 0.2 mg/mL, meaning even dilute concentration can be used for spray coating or spin coating. Ordinary materials are usually mixed with surfactants or stabilizers to form stable ink for inkjet printing, but due to the negatively charged surface, MXene can form stable inks without adding any other chemicals. Water is the most commonly used solvent in the etching process of MAX phase [58], however, due to the abundance of hydrogen bonding, water has a high surface tension of $\sim 72.7 \text{ mN m}^{-1}$, which is higher than most of the substrates such as polyethylene terephthalate (PET, $\sim 48 \text{ mN m}^{-1}$), glass ($\sim 36 \text{ mN m}^{-1}$). Methanol has low surface tension and low boiling points, but MXene is weakly dispersed in the solvent due to their low polarity, thus poor droplet formation due to the low Z . To solve the issue, Zhang et al. first reported the full inkjet printed MSC by using an AlO_x -coated PET substrate ($\sim 66 \text{ mN m}^{-1}$) [131]. Different solvents such as ethanol, DMF, NMP, and DMSO were explored for fine printing. Both high (MXene in NMP, 12.5 mg/mL, $Z \sim 2.2$) and low concentration (MXene in ethanol, 0.7 mg/mL, $Z \sim 2.6$) inks show excellent printing resolution and no “coffee ring” have been observed (Fig. 10a). Interestingly, the adhesion of MXene and substrate is so strong that nothing peels off after a scotch tape peeling test (Fig. 10b). The inkjet-printed lines show low resistance, and resistance shows excellent linearity with printed cycles (Fig. 10c and d). The printed MSC device exhibits a high volumetric capacitance of 562 F/cm^3 and a high energy density of $0.32 \mu\text{Wh cm}^{-2}$, which is claimed to be the highest value for all other printed MSCs (Fig. 10e).

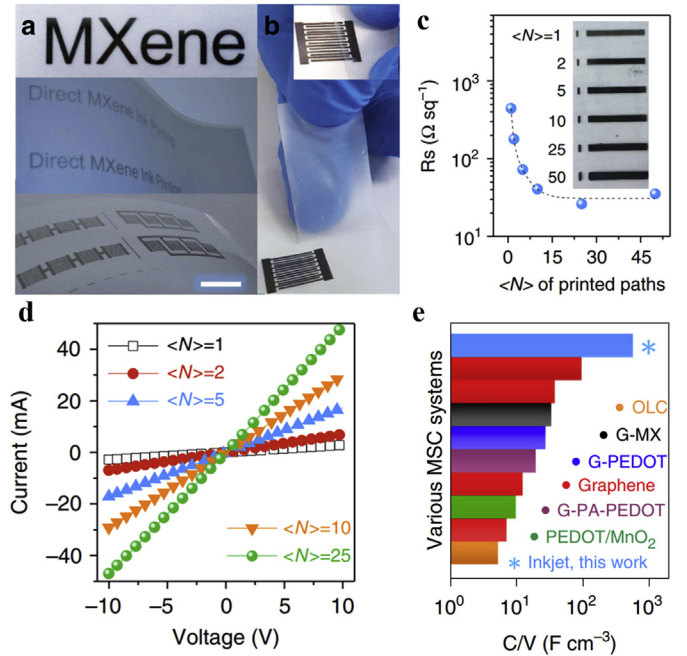


Fig. 10. (a) Optical images of the inkjet-printed MXene MSC in good reproducibility. (b) Optical Image showing peeling test from the scotch tape test. Sheet resistance (c) and IV curve (d) of lines with different cycles. (e) The volumetric capacitance of the inkjet-printed MSC as compared with other reported system. Reprinted with permission from Ref. [131], Copyright 2019 Springer Nature.

4.5. Other fabrication methods

In addition to the fabrication techniques discussed above, there are also several alternative printing techniques that have been explored for the fabrication of MXene MSCs, and a summary of MXene MSCs fabricated by various methods is shown in Table 2. The easiest way is the direct writing of the patterns. For example, Quain et al. developed MXene inks that can be loaded in a rollerball pen for the direct writing of microsupercapacitors or conductive tracks [132]. The writing resolution and thickness of the line can be automated by a computer-controlled robotic arm, a minimum line width of 300 μm has been demonstrated. This direct writing technique can be applied to fabricate MXene MSC in a single step without the need of metal current collector, the MXene pen can be used to write devices on unconventional substrates such as wood, paper, and even a curved cup, and it shows a typical areal capacitance of 5 mF cm^{-2} . A similar concept has been adopted in the extrusion printing of MXene inks [131]. Extrusion printing is a low-cost printing option for a wide of scenarios, it benefits from its high-resolution printing with arbitrary computer-designed shapes and simplicity of printing. The viscous nature of MXene ink enables the fine extrusion printing of MSCs on a variety of substrates such as porous paper and aluminum foil. The printed MXene sheets are strongly adhered onto the substrates without any binders, which benefits from the hydrogen bonding between the layer of sheets. Due to the metallic nature of MXene, the printed lines show a small resistance of 10 $\Omega \text{ sq}^{-1}$ after only 5 times of continuous

printing. As a result, the extrusion-printed MSC device shows excellent mechanical property and reaches a high energy density of 0.32 $\mu\text{Wh cm}^{-2}$ at a power density of 11.4 $\mu\text{W cm}^{-2}$, and it can be further optimized by tuning the line spacings and width. First developed by Zhang et al. [133], stamping is another method for large-scale production of MSCs, it can transfer the materials from the surface of a pre-designed stamp to different substrates such as paper, PET or glass. The stamps can be easily fabricated by 3D-printing, and it can be repeatedly used in the large-scale production line. The final $\text{Ti}_3\text{C}_2\text{T}_x$ MSC device exhibits an areal capacitance of 61 mF cm^{-2} at 25 $\mu\text{A cm}^{-2}$ and retains >80% of its capacitance at 800 $\mu\text{A cm}^{-2}$. This method can even be extended to roll-to-roll printing when proper cylinder stamps are designed.

Automated scalpel patterning is another straightforward method to fabricate the in-plane device, and it is swift, cost-effective, and environmentally friendly. The resolution limitation of this technique relies on the sharpness of the tip and sensitivity of the piezoelectric motor. Salles et al. used the direct engraving technique to pattern solution-processed thin-film MXene MSC [139], MXene thin film was coated on a plasma-treated glass substrate by dip-coating method, the uniformity, and thickness of the film can be controlled by immersion time and pulling rate of the coating process. By using a dull scalpel, they have successfully shown patterns with a resolution of 0.1–0.2 mm. As compared with laser cutting or photolithography, this technique offers direct non-destructive patterning of the solution-processed materials. Li et al. followed this method and reported MXene-conducting polymer electrochromic

Table 2

Summary of MXene-based microsupercapacitor performance.

Preparation Method	Material	Geometry Parameter (μm)			Electrolyte	C_A (mF cm^{-2})	C_V (F cm^{-3})	E_A ($\mu\text{Wh cm}^{-2}$)	P_A (mW cm^{-2})
		W	S	T					
Spray coating + laser cutting [113]	"L-s- $\text{Ti}_3\text{C}_2\text{T}_x$ "	600	110	1.3	PVA/ H_2SO_4	27.3 (20 mV/s)	356.8	2.34–1.43	0.09–1.95
Vacuum filtration + Laser cutting [134]	$\text{Ti}_3\text{C}_2\text{T}_x$	1112	345	4.7	PVA/ H_2SO_4	71.16 (0.5 mA cm^{-2})	151.4	3.52–2.51	0.33–7.99
Spray coating + shadow mask [135]	$\text{Ti}_3\text{C}_2\text{T}_x$	1000	1000	1	PVA/ H_2SO_4	3.26 (5 mV/s)	33	0.34–0.14	0.02–0.16
Stamping [133]	$\text{Ti}_3\text{C}_2\text{T}_x$	415	550	0.69	PVA/ H_2SO_4	61 (25 $\mu\text{A cm}^{-2}$)	884	0.76–0.66	0.01–0.33
Spray coating + Laser cutting [136]	$\text{Ti}_3\text{C}_2\text{T}_x$	1000	1000	4	PVA/ H_3PO_4	23 (0.1 mA cm^{-2})	57.5	1.12–0.92	0.09–0.30
Vacuum filtration + Laser printing [137]	$\text{Ti}_3\text{C}_2\text{T}_x$	745	305	2.2	PVA/ H_2SO_4	27.29 (0.25 mA cm^{-2})	124	1.34–1.21	1.87–3.51
Meyer rod coating + Laser cutting [114]	$\text{Ti}_3\text{C}_2\text{T}_x$	750	450	125	1 M H_2SO_4	25 (20 mV/s)	2	0.77–0.22	7.6–44.6
Vacuum filtration + Oxidative etching [138]	$\text{Ti}_3\text{C}_2\text{T}_x$	200	200	0.52	PVA/ H_2SO_4	0.07 (0.288 A cm^{-3})	1.44	0.01	N/A
Vacuum filtration + Laser cutting [117]	$\text{Ti}_3\text{C}_2\text{T}_x$	N/A	N/A	11	PVA/ H_2SO_4	340 (0.25 mA cm^{-2})	183	13.64–6.16	0.24–4.79
Dip coating + Automated scalpel [139]	$\text{Ti}_3\text{C}_2\text{T}_x$	100	200	0.15	PVA/ H_3PO_4	~0.43 (20 mV/s)	18.9	0.01–0.003	0.001–0.01
Screen printing [120]	$\text{Ti}_3\text{C}_2\text{T}_x$ @ RuO_2	200	100	0.27	PVA/KOH	23.3 (1 mV/s)	864.2	0.36–0.22	0.03–1.31
MEMS technique + Ink injection [107]	$\text{Ti}_3\text{C}_2\text{T}_x$	300	60	300	PVA/ H_3PO_4	276 (20 mV/s)	9.2	28–12	1–8
Extrusion printing [131]	$\text{Ti}_3\text{C}_2\text{T}_x$	438	89	N/A	PVA/ H_2SO_4	43 (5 $\mu\text{A cm}^{-2}$)	N/A	0.32–0.11	0.11–1.58
Inkjet printing [131]	$\text{Ti}_3\text{C}_2\text{T}_x$	80	50	0.21	PVA/ H_2SO_4	12 (4 $\mu\text{A cm}^{-2}$)	562	N/A	N/A
Direct writing [132]	$\text{Ti}_3\text{C}_2\text{T}_x$	N/A	N/A	N/A	PVA/ H_2SO_4	5 (100 mV/s)	N/A	N/A	N/A
Scratch method [140]	$\text{Ti}_3\text{C}_2\text{T}_x$	700	100	8	PVA/ H_3PO_4	25.5 (5 mV/s)	32.2	1.84–1.04	1.28–1.61
Freeze drying + Laser cutting [116]	$\text{Ti}_3\text{C}_2\text{T}_x$ @GO aerogel	N/A	N/A	N/A	PVA/ H_2SO_4	34.6 (1 mV/s)	N/A	2.18–1.33	0.06–0.18
Vacuum filtration with mask [105]	$\text{Ti}_3\text{C}_2\text{T}_x$ @EG	1000	500	3.2	EMIMBF ₄	43.7 (0.2 mA cm^{-2})	35	14	4.5
Vacuum filtration + Laser cutting [115]	$\text{Ti}_3\text{C}_2\text{T}_x$ @BC	1570	295	13.3	PVA/ H_2SO_4	115.2 (0.75 mA cm^{-2})	86.6	5.54	N/A
Spray coating + Scratch [141]	$\text{Ti}_3\text{C}_2\text{T}_x$ @PEDOT	N/A	N/A	0.1	PVA/ H_2SO_4	2.4 (10 mV/s)	240	0.087–0.05	0.0055–0.045
Laser cutting [142]	$\text{Ti}_3\text{C}_2\text{T}_x$	1500	300	90	PVA/LiCl	52 (2 mA cm^{-2})	5.78	2.62	1.26
Laser cutting [142]	$\text{Zn}/\text{Ti}_3\text{C}_2\text{T}_x$	1500	300	N/A	PVA/ $\text{Zn}(\text{CF}_3\text{SO}_3)_2$	66.5 (1 mA cm^{-2})	N/A	N/A	N/A
Spray coating + Laser cut mask [143]	$\text{Ti}_3\text{C}_2\text{T}_x$ //rGO	900	400	0.3	PVA/ H_2SO_4	2.4 (2 mV/s)	80	0.26–0.015	0.06–0.33
Photolithography + Electrodeposition [112]	$\text{Mo}_{1.33}\text{C}/\text{MnO}_2$	N/A	N/A	1.1	PVA/LiCl	69.95 (0.5 mA cm^{-2})	636.9	N/A	N/A
Screen printing [121]	$\text{Ti}_3\text{C}_2\text{T}_x$ //CoAl LDH	1000	1000	N/A	6 M KOH	40 (0.75 mA cm^{-2})	N/A	10.8–8.43	0.34–1.09

GO: Graphene Oxide; PVA: Poly(vinyl acetate) EG: Electrochemically Exfoliated Graphene. LDH: Layered Double Hydroxide; BC: bacterial Cellulose; W, S, T: Width, Spacing, Thickness.

microsupercapacitors by automated scalpel technique [141]. The scratching strategy can also be applied to thick electrodes, and Li et al. reported direct scratching process to fabricate interdigital electrodes from MXene/Electrochemically exfoliated graphene (EG) [140]. The thickness of free-standing films ranges from 3.5 μm to 8 μm , after scratching, interdigital patterns with a width of $\sim 700\ \mu\text{m}$ and an interspace of $\sim 100\ \mu\text{m}$ can be obtained. They have shown that even a smaller interspace of 15 μm can be achieved by changing the diameter of the scratching needle.

Mask-assisted deposition technique has proven to be another effective way to convert MXene inks into interdigital patterns. For instance, Hu et al. fabricated all-solid-state MXene MSC by combining the vacuum filtration method with laser-printed electrode templates [137]. The electrode template mask can be efficiently designed and printed by an ordinary office laser printer. After MXene suspension has been deposited by vacuum-assisted deposition, interdigital patterns can be formed after a lift-off process in tetrahydrofuran. As a result, the final symmetric MXene MSC shows a maximum areal capacitance of 27.29 mF cm^{-2} . Zheng et al. further demonstrated that the vacuum filtrated MXene could be transferred onto flexible polyethylene terephthalate (PET) substrate [105]. A thin bottom layer of EG is proved to be critical for the successful transfer of the MXene layer without short circuits. The final device shows excellent flexibility and sustains superior performance under different deformation conditions such as bending and twisting. This method is simple and versatile for the fabrication of flexible MSCs, and it is compatible with a range of other 2D materials [144,145].

As another new family of MSCs, fiber shaped MSCs with unique 1D fibers as electrodes have attracted significant interest since 2011 and have shown great application potential in miniaturized electronics and wearable electronics. The fabrication of fiber electrodes is constrained by the geometrical and mechanical flexibility requirement of the fibers. MXene-based fiber shaped MSCs have been obtained by the following methods: 1) mild baking method, 2) electrospinning method, 3) wet-spinning method, 4) drop-casting method. The mild baking method is utilized to deposit MXene on the fibers by the removal of the solvent. For example, Hu et al. employed $\text{Ti}_3\text{C}_2\text{T}_x$ MXene to fabricate all-solid-state

flexible fiber-based MSCs [146], in which two $\text{Ti}_3\text{C}_2\text{T}_x$ @silver-plated nylon fiber electrodes were embedded in parallel into a PVA- H_2SO_4 hydrogel (Fig. 11a). The as-prepared $\text{Ti}_3\text{C}_2\text{T}_x$ suspension was loaded dropwise on the functionalized silver-plated nylon fibers that were placed on a hot plate. With the removal of water upon mild baking, $\text{Ti}_3\text{C}_2\text{T}_x$ was left behind on the fibers as the active material (Fig. 11b). The fabricated device exhibited a high areal capacitance of 328 mF cm^{-2} with excellent cyclability, flexibility, electrochemical stability and mechanical stability (Fig. 11c–f). Through a similar method, MXene can also be deposited on carbonized silk with good capacitance retention in a bending state of 120° [147].

$\text{Ti}_3\text{C}_2\text{T}_x$ can also be sprayed onto polyester (PET) fibers by electrospinning method. $\text{Ti}_3\text{C}_2\text{T}_x$ can be uniformly self-wounded on PET yarn [148]; the final device shows high capacity retention under different bending conditions. Yang et al. reported a wet-spinning assembly strategy for the continuous fabrication of MXene/rGO fibers through a synergistic effect between graphene oxides liquid crystals and MXene sheets [149]. The synergistic contribution of rGO and MXene (10% in weight) results in a tensile strength of $\sim 145\ \text{MPa}$, while MXene/rGO with 90% MXene content has a tensile strength of only 12.9 MPa. Excellent overall fiber electrical conductivity and superior volumetric capacitance of the integrated supercapacitor were achieved. The drop-casting method is employed to deposit MXene on a base with excellent flexibility. $\text{Ti}_3\text{C}_2\text{T}_x$ /PEDOT-PSS coated carbon fibers (CF) display robust performance under various mechanical deformations [150].

In addition, different from conventional core (conductive fiber)–shell (active nanomaterials) fibrous structure [151], $\text{Ti}_3\text{C}_2\text{T}_x$ /CNTs film has been rolled into a fiber with helical structure by hosting $\text{Ti}_3\text{C}_2\text{T}_x$ nanosheets in the corridor of a scrolled carbon nanotube scaffold, which is assembled into a special supercapacitor (Fig. 12a and b), and the capacity retention is 99% without bending, and 98% under bending after 1500 cycles (Fig. 12c and d).

5. Conclusion and perspective

Microsupercapacitors are a promising energy storage solution for

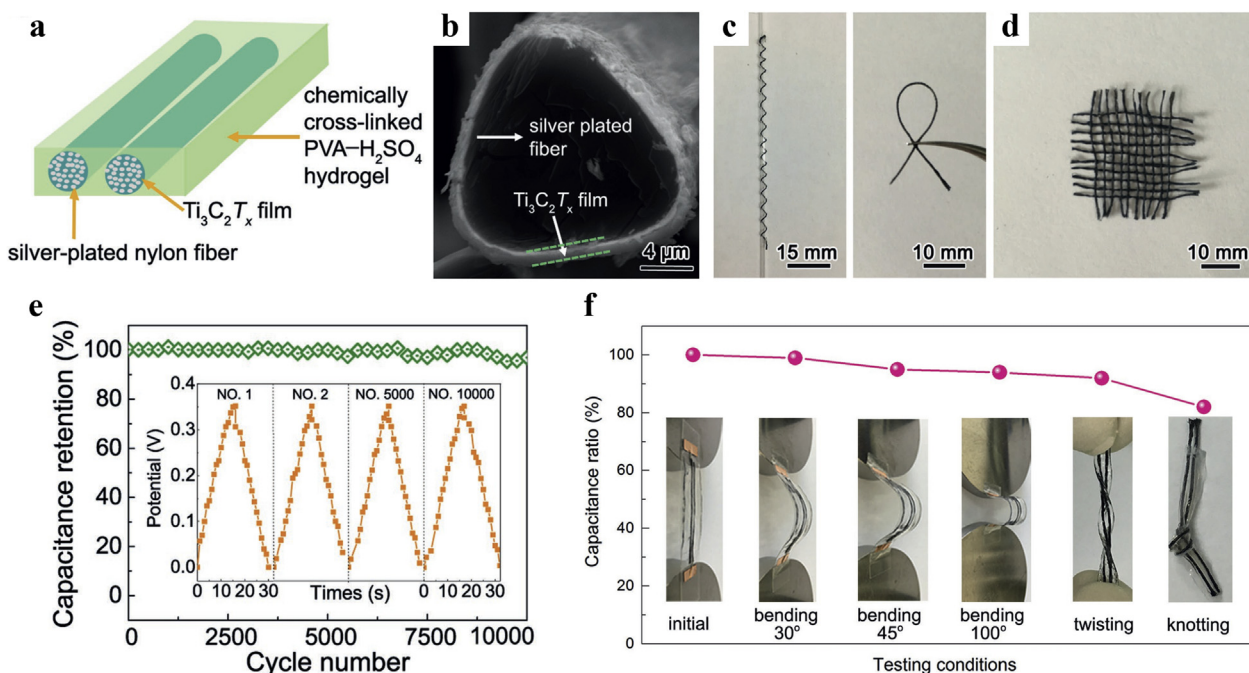


Fig. 11. (a) Schematic of the assembled all-solid-state fiber-based supercapacitor device. (b) SEM cross-sectional image of well fabricated $\text{Ti}_3\text{C}_2\text{T}_x$ films coating the entire fibers. (c) Planar structures and (d) textile fabric obtained by twisting or knitting fibers. (e) Capacitance retention test of the fiber-based SC device. Inset shows galvanostatic cycling data. (f) Normalized capacitance (C/C_0 , where C_0 is the initial capacitance) of the all-solid-state fiber-based supercapacitor under various deformation modes at a scan rate of 20 mV/s. Reproduced with permission [146]. Copyright 2017, Wiley-VCH.

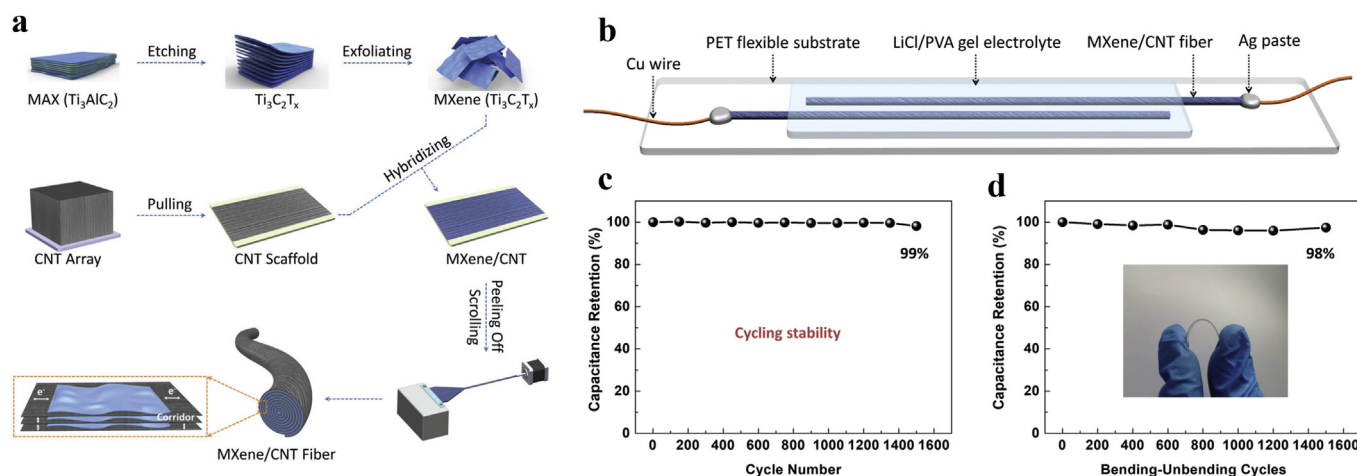


Fig. 12. (a) Schematic illustration of the preparation of host (CNTs)-guest (MXenes) hybrid fiber with a helical structure. (b) Schematic illustration showing the structure of fiber-based supercapacitor. (c) Cycling stability and (d) mechanical flexibility of the supercapacitor made of MXene/CNT fiber with 90 wt% of MXene nanosheets. The inset in (d) shows the photograph of a fiber-shaped supercapacitor in bending state. Reproduced with permission [151]. Copyright 2018, Wiley-VCH.

miniaturized electronics and wireless sensor networks. However, for practical use, achieving high energy and power densities in a given footprint area is still challenging. MXenes show promising advantages over other electrode materials used in MSC devices due to their high conductivity, high volumetric capacitance, ease of processing and excellent mechanical flexibility. Numerous fabrication techniques have been explored and significant progress has been made in the fabrication of MXene MSCs; however, it should also be noted that the development of MXene MSCs is still only in its infancy and more insights into the material development and device optimization need to be considered.

Currently, significant efforts have been focused on the improvement of the areal energy and power densities of MSCs, while the self-discharge characteristics of MSC are neglected. The self-discharge phenomenon causes a rapid voltage drop, and MSCs lose their charges quickly in open circuit. Unlike energy storage in regenerative braking or other applications where self-discharge is not a significant issue, MSC is designed to be integrated with small electronics. Thus, they should have the ability to store charges in the long-term. We are the first group to report the self-discharge rate of MXene MSC and demonstrated its practical application [136]. Other literature has recently been published to suppress the self-discharge of supercapacitor, and similar methods are worth to be tried to the MXene MSCs [152,153]. Charge re-distribution models have been established to explain the self-discharge phenomenon for EDLCs [154–157], but how these models fit pseudocapacitors such as MXenes are not clear at present.

Solid-state or quasi-solid-state electrolytes have attracted considerable attention in MSC applications due to their simplicity of encapsulation and free of electrolyte leakage. Gel polymer electrolyte is the most extensively used electrolyte in MXene MSCs, and it consists of a polymer host (usually PVA) and an aqueous electrolyte (usually H₂SO₄), polymers matrix swells by the solvent and ions can transport in the electrolyte. However, the hydrogels with aqueous electrolytes have a small voltage window, which is limited by electrolyte decomposition, including the hydrogen and the oxygen evolution reactions. To expand the working potential windows, different organic solvents such as polycarbonate (PC) [158], ethylene carbonate (EC), dimethylformamide (DMF) [159] and acetonitrile [160] can also be examined as plasticizers, and cell voltage can be increased to 2.5–3 V. The selection of salt, host polymer, solvent, and the proper ratio among them are critical to achieving high electrochemical performance. Apart from this, ionogel is another type of quasi-solid electrolyte where ionic liquids are incorporated into the appropriate polymer matrix under a polycondensation process [161–163], their excellent thermal stability enables wider operational temperatures of the microdevices. While symmetric MXene-based MSC is

often limited by the low voltage of operation (0.6 V) due to oxidation of positive MXene electrodes at anodic potentials. So, efforts need to be put forward in designing asymmetric MXene devices with enlarged voltage windows. Similarly, in non-aqueous electrolytes, MXene based asymmetric devices need to be developed for high voltage window of operation above 3 V with excellent cycling stability [164]. Besides, there is a lot of room for exploring a variety of cations including Na⁺, Zn²⁺, Al³⁺ hybrid metal capacitors as MXene galleries spontaneously intercalate cations while positive electrodes such as carbons, metal oxides, and conductive polymers can be paired with.

Areal energy density is mainly relying on the areal mass loading of the active material. However, similar to other 2D materials, converting MXene flakes into thick films results in the restacking of the flakes and decrease the accessible active sites to the electrolyte ions. To solve the restacking problem, different spacers such as CNT [165], polyvinyl alcohol [45], Polyaniline [166], Polypyrrole [167] or nanostructure metal oxides [168] have been introduced between MXene layers. The agglomeration of the MXene layers could be improved by the electroactive spacers, resulting in a more accessible surface area of the electrode material. Thus, the technological operation needs to be further developed to be compatible with those composite materials, which sometimes are in the form of powders instead of inks. The restacking problem could be also alleviated by designing 3D current collectors with porous architectures. The porous 3D structures not only create paths for electrolyte penetration but also facilitate the transport of electrons because they act as 3D current collectors, ensuring simultaneous low electrical resistance and high capacitance. Besides, the vertical-aligned MXene electrode was achieved and showed excellent thickness-independent performance up to 200 μm [169]. Transferring the vertically aligned MXene film to MSC patterns is an attractive solution for high-energy-density MSC.

MXene family has expanded rapidly since its first discovery in 2011. Although more than 20 different MXenes have been experimentally synthesized, only Ti₃C₂T_x has been extensively explored as electrodes for MSCs. There is an excellent potential to search for new MXenes with different functionalities to develop advanced MSCs. For example, Ti₂C should theoretically exhibit higher gravimetric capacitance than Ti₃C₂ because more Ti atom layers are exposed to the electrolyte. Mo_{1.33}C with ordered metal divacancies shows a volumetric of 1100 F/cm³ and high conductivity of ~29000 S/m [92]. Vanadium carbide MXene shows a gravimetric capacitance of 487 F/g in the acid electrolytes [94]. Further optimization of these materials may be combined with computational studies to discover new promising directions. MXene quantum dots (MQDs) are another promising class of MXene-based materials due to their novel physical and chemical properties. MQDs are widely used in

optical, photocatalytic, biomedical, and cellular imaging areas [170–172]. Compared with 2D MXene sheets, MQDs own special properties including ultrasmall size, chemical stability, exceptional electrical conductivity, and abundance of edge defects, those unique properties may open the door to their applications in MSCs.

Declaration of competing interest

The authors declare that they have no known competing financial interests or personal relationships that could have appeared to influence the work reported in this paper.

CRediT authorship contribution statement

Qiu Jiang: Conceptualization, Writing - original draft. **Yongjiu Lei:** Writing - original draft, Writing - review & editing. **Hanfeng Liang:** Writing - review & editing. **Kai Xi:** Writing - review & editing. **Chuan Xia:** Conceptualization, Supervision. **Husam N. Alshareef:** Conceptualization, Supervision, Funding acquisition.

Acknowledgments

This work is supported by King Abdullah University of Science and Technology (KAUST). Authors thank Narendra Kurra (Drexel University) for helpful comments on the manuscript.

References

- [1] M.R. Palattella, M. Dohler, A. Grieco, G. Rizzo, J. Torsner, T. Engel, L. Ladid, Internet of Things in the 5G Era: enablers, architecture, and business models, *IEEE J. Sel. Area. Commun.* 34 (2016) 510–527, <https://doi.org/10.1109/JSAC.2016.2525418>.
- [2] C. Wu, A.C. Wang, W. Ding, H. Guo, Z.L. Wang, Triboelectric nanogenerator: a foundation of the energy for the New Era, *Adv. Energy Mater.* 9 (2019) 1–25, <https://doi.org/10.1002/aenm.201802906>.
- [3] N.A. Kyeremateng, T. Brousse, D. Pech, Microsupercapacitors as miniaturized energy-storage components for on-chip electronics, *Nat. Nanotechnol.* 12 (2017) 7–15, <https://doi.org/10.1038/nnano.2016.196>.
- [4] J.W. Long, B. Dunn, D.R. Rolison, H.S. White, Three-dimensional battery architectures, *Chem. Rev.* 104 (2004) 4463–4492, <https://doi.org/10.1021/cr020740l>.
- [5] M. Beidaghi, Y. Gogotsi, Capacitive energy storage in micro-scale devices: recent advances in design and fabrication of micro-supercapacitors, *Energy Environ. Sci.* 7 (2014) 867, <https://doi.org/10.1039/c3ee43526a>.
- [6] S. Zheng, X. Shi, P. Das, Z.S. Wu, X. Bao, The road towards planar microbatteries and micro-supercapacitors: from 2D to 3D device geometries, *Adv. Mater.* 31 (2019) 1900583, <https://doi.org/10.1002/adma.201900583>.
- [7] D. Yu, K. Goh, Q. Zhang, L. Wei, H. Wang, W. Jiang, Y. Chen, Controlled functionalization of carbonaceous fibers for asymmetric solid-state micro-supercapacitors with high volumetric energy density, *Adv. Mater.* 26 (2014) 6790–6797, <https://doi.org/10.1002/adma.201403061>.
- [8] B. Zheng, T. Huang, L. Kou, X. Zhao, K. Gopalsamy, C. Gao, Graphene fiber-based asymmetric micro-supercapacitors, *J. Mater. Chem. A* 2 (2014) 9736–9743, <https://doi.org/10.1039/c4ta01868k>.
- [9] Z. Cai, L. Li, J. Ren, L. Qiu, H. Lin, H. Peng, Flexible, weavable and efficient microsupercapacitor wires based on polyaniline composite fibers incorporated with aligned carbon nanotubes, *J. Mater. Chem. A* 1 (2013) 258–261, <https://doi.org/10.1039/c2ta00274d>.
- [10] J. Chmiola, P.L.T. Celine Largeot, P. Simon, Y. Gogotsi, Monolithic carbide-derived carbon films for micro-supercapacitors, *Science* 328 (2010) 480–483, <https://doi.org/10.1126/science.1184126>.
- [11] D. Pech, M. Brunet, H. Durou, P. Huang, V. Mochalin, Y. Gogotsi, P.L. Taberna, P. Simon, Ultrahigh-power micrometre-sized supercapacitors based on onion-like carbon, *Nat. Nanotechnol.* 5 (2010) 651–654, <https://doi.org/10.1038/nnano.2010.162>.
- [12] D. Pech, M. Brunet, P.L. Taberna, P. Simon, N. Fabre, F. Mesnilgrente, V. Conédéra, H. Durou, Elaboration of a microstructured inkjet-printed carbon electrochemical capacitor, *J. Power Sources* 195 (2010) 1266–1269, <https://doi.org/10.1016/j.jpowsour.2009.08.085>.
- [13] B. Hsia, M.S. Kim, M. Vincent, C. Carraro, R. Maboudian, Photoresist-derived porous carbon for on-chip micro-supercapacitors, *Carbon* 57 (2013) 395–400, <https://doi.org/10.1016/j.carbon.2013.01.089>.
- [14] M. Beidaghi, W. Chen, C. Wang, Electrochemically activated carbon micro-electrode arrays for electrochemical micro-capacitors, *J. Power Sources* 196 (2011) 2403–2409, <https://doi.org/10.1016/j.jpowsour.2010.09.050>.
- [15] S. Wang, B. Hsia, C. Carraro, R. Maboudian, High-performance all solid-state micro-supercapacitor based on patterned photoresist-derived porous carbon electrodes and an ionogel electrolyte, *J. Mater. Chem. A* 2 (2014) 7997–8002, <https://doi.org/10.1039/C4TA00570H>.
- [16] M.S. Kim, B. Hsia, C. Carraro, R. Maboudian, Flexible micro-supercapacitors with high energy density from simple transfer of photoresist-derived porous carbon electrodes, *Carbon* 74 (2014) 163–169, <https://doi.org/10.1016/j.carbon.2014.03.019>.
- [17] M. Beidaghi, C. Wang, Micro-supercapacitors based on interdigital electrodes of reduced graphene oxide and carbon nanotube composites with ultrahigh power handling performance, *Adv. Funct. Mater.* 22 (2012) 4501–4510, <https://doi.org/10.1002/adfm.201201292>.
- [18] J. Lin, C. Zhang, Z. Yan, Y. Zhu, Z. Peng, R.H. Hauge, D. Natelson, J.M. Tour, 3-Dimensional graphene carbon nanotube carpet-based microsupercapacitors with high electrochemical performance, *Nano Lett.* 13 (2013) 72–78, <https://doi.org/10.1021/nl3034976>.
- [19] G. Xiong, C. Meng, R.G. Reifenger, P.P. Irazoqui, T.S. Fisher, Graphitic petal micro-supercapacitor electrodes for ultra-high power density, *Energy Technol.* 2 (2014) 897–905, <https://doi.org/10.1002/ente.201402055>.
- [20] J. Liang, A.K. Mondal, D.W. Wang, F. Iacopi, Graphene-based planar micro-supercapacitors: recent advances and future challenges, *Adv. Mater. Technol.* 4 (2019) 1–38, <https://doi.org/10.1002/admt.201800200>.
- [21] G. Zhang, Y. Han, C. Shao, N. Chen, G. Sun, X. Jin, J. Gao, B. Ji, H. Yang, L. Qu, Processing and manufacturing of graphene-based microsupercapacitors, *Mater. Chem. Front.* 2 (2018) 1750–1764, <https://doi.org/10.1039/c8qm00270c>.
- [22] N. Kurra, Q. Jiang, P. Nayak, H.N. Alshareef, Laser-derived graphene: a three-dimensional printed graphene electrode and its emerging applications, *Nano Today* 24 (2019) 81–102, <https://doi.org/10.1016/j.nantod.2018.12.003>.
- [23] N. Kurra, M.K. Hota, H.N. Alshareef, Conducting polymer micro-supercapacitors for flexible energy storage and AC line-filtering, *Nano Energy* 13 (2015) 500–508, <https://doi.org/10.1016/j.nanoen.2015.03.018>.
- [24] M. Beidaghi, C. Wang, Micro-supercapacitors based on three dimensional interdigital polypyrrole/C-MEMS electrodes, *Electrochim. Acta* 56 (2011) 9508–9514, <https://doi.org/10.1016/j.electacta.2011.08.054>.
- [25] C. Meng, J. Maeng, S.W.M. John, P.P. Irazoqui, Ultrasmall integrated 3d micro-supercapacitors solve energy storage for miniature devices, *Adv. Energy Mater.* 4 (2014) 1301269, <https://doi.org/10.1002/aenm.201301269>.
- [26] K. Wang, W. Zou, B. Quan, A. Yu, H. Wu, P. Jiang, Z. Wei, An all-solid-state flexible micro-supercapacitor on a chip, *Adv. Energy Mater.* 1 (2011) 1068–1072, <https://doi.org/10.1002/aenm.201100488>.
- [27] T.M. Dinh, K. Armstrong, D. Guay, D. Pech, High-resolution on-chip supercapacitors with ultra-high scan rate ability, *J. Mater. Chem. A* 2 (2014) 7170–7174, <https://doi.org/10.1039/C4TA00640B>.
- [28] W. Shi, C. Yan, Y. Chen, S. Oswald, L. Han, O.G. Schmidt, On-chip, all-solid-state and flexible micro-supercapacitors with high performance based on MnO₂/Au multilayers, *Energy Environ. Sci.* 6 (2013) 3218–3223, <https://doi.org/10.1039/c3ee41286e>.
- [29] T. Brezesinski, J. Wang, S.H. Tolbert, B. Dunn, Ordered mesoporous α -MoO₃ with iso-oriented nanocrystalline walls for thin-film pseudocapacitors, *Nat. Mater.* 9 (2010) 146–151, <https://doi.org/10.1038/nmat2612>.
- [30] V. Augustyn, J. Come, M.A. Lowe, J.W. Kim, P. Taberna, S.H. Tolbert, H.D. Abruna, P. Simon, B. Dunn, High-rate electrochemical energy storage through Li⁺ intercalation pseudocapacitance 12 (2013) 518–522, <https://doi.org/10.1038/nmat3601>.
- [31] D. Choi, G.E. Blomgren, P.N. Kumta, Fast and reversible surface redox reaction in nanocrystalline vanadium nitride supercapacitors, *Adv. Mater.* 18 (2006) 1178–1182, <https://doi.org/10.1002/adma.200502471>.
- [32] S. Lu, T. Zhu, H. Wu, Y. Wang, J. Li, A. Abdelkader, K. Xi, W. Wang, Y. Li, S. Ding, G. Gao, R.V. Kumar, Construction of ultrafine ZnSe nanoparticles on/in amorphous carbon hollow nanospheres with high-power-density sodium storage, *Nano Energy* 59 (2019) 762–772, <https://doi.org/10.1016/j.nanoen.2019.03.008>.
- [33] J. Liang, K. Xi, G. Tan, S. Chen, T. Zhao, P.R. Coxon, H.K. Kim, S. Ding, Y. Yang, R.V. Kumar, J. Lu, Sea urchin-like NiCo₂O₄/C nanocomposites for Li-ion batteries and supercapacitors, *Nano Energy* 27 (2016) 457–465, <https://doi.org/10.1016/j.nanoen.2016.06.032>.
- [34] J. Yang, Z. Pan, Q. Yu, Q. Zhang, X. Ding, X. Shi, Y. Qiu, K. Zhang, J. Wang, Y. Zhang, Free-standing black phosphorus thin films for flexible quasi-solid-state micro-supercapacitors with high volumetric power and energy density, *ACS Appl. Mater. Interfaces* 11 (2019) 5938–5946, <https://doi.org/10.1021/acsami.8b18172>.
- [35] H. Wu, W. Zhang, S. Kandambeth, O. Shekhar, M. Eddaoudi, H.N. Alshareef, Conductive metal-organic frameworks selectively grown on laser-scribed graphene for electrochemical microsupercapacitors, *Adv. Energy Mater.* 9 (2019) 1900482, <https://doi.org/10.1002/aenm.201900482>.
- [36] N. Kurra, C. Xia, M.N. Hedhili, H.N. Alshareef, Ternary chalcogenide micro-pseudocapacitors for on-chip energy storage, *Chem. Commun.* 51 (2015) 10494–10497, <https://doi.org/10.1039/C5CC03220B>.
- [37] Y. Gogotsi, B. Anasori, The rise of MXenes, *ACS Nano* 13 (2019) 8491–8494, <https://doi.org/10.1021/acsnano.9b06394>.
- [38] J.L. Hart, K. Hantanasirisakul, A.C. Lang, B. Anasori, D. Pinto, Y. Pivak, J.T. van Ommen, S.J. May, Y. Gogotsi, M.L. Taheri, Control of MXenes' electronic properties through termination and intercalation, *Nat. Commun.* 10 (2019), <https://doi.org/10.1038/s41467-018-08169-8>.
- [39] C.F. John Zhang, V. Nicolosi, Graphene and MXene-based transparent conductive electrodes and supercapacitors, *Energy Storage Mater* 16 (2019) 102–125, <https://doi.org/10.1016/j.ensm.2018.05.003>.

- [40] M. Naguib, M. Kurtoglu, V. Presser, J. Lu, J. Niu, M. Heon, L. Hultman, Y. Gogotsi, M.W. Barsoum, Two-dimensional nanocrystals produced by exfoliation of Ti_3AlC_2 , *Adv. Mater.* 23 (2011) 4248–4253, <https://doi.org/10.1002/adma.201102306>.
- [41] H. Kim, Z. Wang, H.N. Alshareef, MXenes: electronic and photonic applications of MXenes, *Nano Energy* 60 (2019) 179–197, <https://doi.org/10.1016/j.nanoen.2019.03.020>.
- [42] Y. Zhong, X.H. Xia, F. Shi, J.Y. Zhan, J.P. Tu, H.J. Fan, Transition metal carbides and nitrides in energy storage and conversion, *Adv. Sci.* 3 (2015) 1500286, <https://doi.org/10.1002/advs.201500286>.
- [43] B. Anasori, M.R. Lukatskaya, Y. Gogotsi, 2D metal carbides and nitrides (MXenes) for energy storage, *Nat. Rev. Mater.* 2 (2017) 16098, <https://doi.org/10.1038/natrevmats.2016.98>.
- [44] M. Naguib, V.N. Mochalin, M.W. Barsoum, Y. Gogotsi, 25th anniversary article: MXenes: a new family of two-dimensional materials, *Adv. Mater.* 26 (2014) 992–1005, <https://doi.org/10.1002/adma.201304138>.
- [45] Z. Ling, C.E. Ren, M.Q. Zhao, J. Yang, J.M. Giammarco, J. Qiu, M.W. Barsoum, Y. Gogotsi, Flexible and conductive MXene films and nanocomposites with high capacitance, *Proc. Natl. Acad. Sci. U. S. A.* 111 (2014) 16676–16681, <https://doi.org/10.1073/pnas.1414215111>.
- [46] M.R. Lukatskaya, S. Kota, Z. Lin, M.Q. Zhao, N. Shpigel, M.D. Levi, J. Halim, P.L. Taberna, M.W. Barsoum, P. Simon, Y. Gogotsi, Ultra-high-rate pseudocapacitive energy storage in two-dimensional transition metal carbides, *Nat. Energy* 6 (2017) 17105, <https://doi.org/10.1038/nenergy.2017.105>.
- [47] Z.S. Wu, X. Feng, H.M. Cheng, Recent advances in graphene-based planar micro-supercapacitors for on-chip energy storage, *Natl. Sci. Rev.* 1 (2014) 277–292, <https://doi.org/10.1093/nsr/nwt003>.
- [48] Y. Yoon, W. Cho, J. Lim, D. Choi, Solid-state thin-film supercapacitor with ruthenium oxide and solid electrolyte thin films, *J. Power Sources* 101 (2001) 126–129, [https://doi.org/10.1016/S0378-7753\(01\)00484-0](https://doi.org/10.1016/S0378-7753(01)00484-0).
- [49] J.H. Lim, D.J. Choi, H.K. Kim, W.I. Cho, Y.S. Yoon, Thin film supercapacitors using a sputtered RuO_2 electrode, *J. Electrochem. Soc.* 148 (2001) 275–278, <https://doi.org/10.1149/1.1350666>.
- [50] M.K. Hota, Q. Jiang, Y. Mashraei, K.N. Salama, H.N. Alshareef, Fractal electrochemical microsupercapacitors, *Adv. Electron. Mater.* 3 (2017), <https://doi.org/10.1002/aeml.201700185>.
- [51] Y. Gogotsi, R.M. Penner, Energy storage in nanomaterials – capacitive, pseudocapacitive, or battery-like? *ACS Nano* 12 (2018) 2081–2083, <https://doi.org/10.1021/acsnano.8b01914>.
- [52] P. Simon, Y. Gogotsi, B. Dunn, Where do batteries end and supercapacitors begin? *Science* 343 (2014) 1210–1211, <https://doi.org/10.1126/science.1249625>.
- [53] T. Brousse, B. Daniel, To Be or not to Be Pseudocapacitive? <http://doi.org/10.1149/2.0201505jes>, 2015, 162, 5185–5189.
- [54] A. Balducci, D. Belanger, T. Brousse, J.W. Long, W. Sugimoto, Perspective—a guideline for reporting performance metrics with electrochemical capacitors: from electrode materials to full devices, *J. Electrochem. Soc.* 164 (2017) 1487–1488, <https://doi.org/10.1149/2.0851707jes>.
- [55] M. Hu, Z. Li, T. Hu, S. Zhu, C. Zhang, X. Wang, High-capacitance mechanism for $\text{Ti}_3\text{C}_2\text{T}_x$ MXene by in situ electrochemical Raman spectroscopy investigation, *ACS Nano* 10 (2016) 11344–11350, <https://doi.org/10.1021/acsnano.6b06597>.
- [56] A. Laheäär, P. Przygocki, Q. Abbas, F. Béguin, Appropriate methods for evaluating the efficiency and capacitive behavior of different types of supercapacitors, *Electrochem. Commun.* 60 (2015) 21–25, <https://doi.org/10.1016/j.elecom.2015.07.022>.
- [57] T.S. Mathis, N. Kurra, X. Wang, D. Pinto, P. Simon, Energy storage data reporting in perspective — guidelines for interpreting the performance of electrochemical energy storage systems. <http://doi.org/10.1002/aenm.201902007>, 2019, 9, 1902007.
- [58] L. Verger, V. Natu, M. Carey, M.W. Barsoum, MXenes: an introduction of their synthesis, select properties, and applications, *Trends Chem* 1 (2019) 657–669, <https://doi.org/10.1016/j.trechm.2019.04.006>.
- [59] L.H. Karlsson, J. Birch, J. Halim, M.W. Barsoum, P.O. Å. Persson, Atomically resolved structural and chemical investigation of single MXene sheets, *Nano Lett.* 15 (2015) 4955–4960, <https://doi.org/10.1021/acs.nanolett.5b00737>.
- [60] M. Ghidui, M.R. Lukatskaya, M.Q. Zhao, Y. Gogotsi, M.W. Barsoum, Conductive two-dimensional titanium carbide “clay” with high volumetric capacitance, *Nature* 516 (2015) 78–81, <https://doi.org/10.1038/nature13970>.
- [61] T. Li, L. Yao, Q. Liu, J. Gu, R. Luo, J. Li, X. Yan, W. Wang, P. Liu, B. Chen, W. Zhang, W. Abbas, R. Naz, D. Zhang, Fluorine-free synthesis of high-purity $\text{Ti}_3\text{C}_2\text{T}_x$ ($\text{T}=\text{OH}$, O) via alkali treatment, *Angew. Chem. Int. Ed.* 57 (2018) 6115–6119, <https://doi.org/10.1002/anie.201800887>.
- [62] C. Peng, P. Wei, X. Chen, Y. Zhang, F. Zhu, Y. Cao, H. Wang, H. Yu, F. Peng, A hydrothermal etching route to synthesis of 2D MXene (Ti_3C_2 , Nb_2C): enhanced exfoliation and improved adsorption performance, *Ceram. Int.* 44 (2018), <https://doi.org/10.1016/j.ceramint.2018.07.124>, 18886–18893.
- [63] M. Li, J. Lu, K. Luo, Y. Li, K. Chang, K. Chen, J. Zhou, J. Rosen, L. Hultman, P. Eklund, P.O. Å. Persson, S. Du, Z. Chai, Z. Huang, Q. Huang, Element replacement approach by reaction with lewis acidic molten salts to synthesize nanolaminated MAX phases and MXenes, *J. Am. Chem. Soc.* 141 (2019) 4730–4737, <https://doi.org/10.1021/jacs.9b00574>.
- [64] W. Sun, S. Shah, Y. Chen, Z. Tan, H. Gao, T. Habib, M. Radovic, M. Green, Electrochemical etching of Ti_2AlC to Ti_2CT_x (MXene) in low-concentration hydrochloric acid solution, *J. Mater. Chem. A* 5 (2017) 21663–21668, <https://doi.org/10.1039/C7TA05574A>.
- [65] S. Yang, P. Zhang, F. Wang, A.G. Ricciardulli, M.R. Lohe, P.W.M. Blom, X. Feng, Fluoride-free synthesis of two-dimensional titanium carbide (MXene) using a binary aqueous system, *Angew. Chem. Int. Ed.* 57 (2018) 15491–15495, <https://doi.org/10.1002/anie.201809662>.
- [66] O. Mashtalir, M. Naguib, V.N. Mochalin, Y. Dall’Agnese, M. Heon, M.W. Barsoum, Y. Gogotsi, Intercalation and delamination of layered carbides and carbonitrides, *Nat. Commun.* 4 (2013) 1716, <https://doi.org/10.1038/ncomms2664>.
- [67] Y. Xu, T. Wang, C. Yang, R. Wang, A high-performance flexible pseudo-supercapacitor constructed on conductive cloth, 2016 17th, Int. Conf. Electron. Packag. Technol. ICEPT (2016) 133–137, <https://doi.org/10.1109/ICEPT.2016.7583105>, 2016.
- [68] M. Ghidui, J. Halim, S. Kota, D. Bish, Y. Gogotsi, M.W. Barsoum, Ion-exchange and cation solvation reactions in Ti_3C_2 MXene, *Chem. Mater.* 28 (2016) 3507–3514, <https://doi.org/10.1021/acs.chemmater.6b01275>.
- [69] A. Sarycheva, A. Polemi, Y. Liu, K. Dandekar, B. Anasori, Y. Gogotsi, 2D titanium carbide (MXene) for wireless communication, *Sci. Adv.* 4 (2018), <https://doi.org/10.1126/sciadv.aau0920> eaau0920.
- [70] M. Alhabeb, K. Maleski, B. Anasori, P. Lelyukh, L. Clark, S. Sin, Y. Gogotsi, Guidelines for synthesis and processing of 2D titanium carbide ($\text{Ti}_3\text{C}_2\text{T}_x$ MXene), *Chem. Mater.* 18 (2017) 7633–7644, <https://doi.org/10.1021/acs.chemmater.7b02847>.
- [71] X. Wang, X. Shen, Y. Gao, Z. Wang, R. Yu, L. Chen, Atomic-scale recognition of surface structure and intercalation mechanism of $\text{Ti}_3\text{C}_2\text{T}_x$, *J. Am. Chem. Soc.* 137 (2015) 2715–2721, <https://doi.org/10.1021/ja512820k>.
- [72] Q. Jiang, N. Kurra, M. Alhabeb, Y. Gogotsi, H.N. Alshareef, All pseudocapacitive MXene- RuO_2 asymmetric supercapacitors, *Adv. Energy Mater.* 8 (2018) 1703043, <https://doi.org/10.1002/aenm.201703043>.
- [73] M. Kurtoglu, M. Naguib, Y. Gogotsi, M.W. Barsoum, First principles study of two-dimensional early transition metal carbides, *MRS Commun* 2 (2012) 133–137, <https://doi.org/10.1557/mrc.2012.25>.
- [74] M. Khazaei, M. Arai, T. Sasaki, C.Y. Chung, N.S. Venkataraman, M. Estili, Y. Sakka, Y. Kawazoe, Novel electronic and magnetic properties of two-dimensional transition metal carbides and nitrides, *Adv. Funct. Mater.* 23 (2013) 2185–2192, <https://doi.org/10.1002/adfm.201202502>.
- [75] M. Khazaei, M. Arai, T. Sasaki, M. Estili, Y. Sakka, Two-dimensional molybdenum carbides: potential thermoelectric materials of the MXene family, *Phys. Chem. Chem. Phys.* 16 (2014) 7841–7849, <https://doi.org/10.1039/c4cp00467a>.
- [76] B. Anasori, C. Shi, E.J. Moon, Y. Xie, C.A. Voigt, P.R.C. Kent, S.J. May, S.J.L. Billinge, M.W. Barsoum, Y. Gogotsi, Control of electronic properties of 2D carbides (MXenes) by manipulating their transition metal layers, *Nanoscale Horizons* 1 (2016) 227–234, <https://doi.org/10.1039/c5nh00125k>.
- [77] M. Khazaei, A. Ranjbar, M. Arai, T. Sasaki, S. Yunoki, Electronic properties and applications of MXenes: a theoretical review, *J. Mater. Chem. C* 5 (2017) 2488–2503, <https://doi.org/10.1039/c7tc00140a>.
- [78] M. Ashton, K. Mathew, R.G. Hennig, S.B. Sinnott, Predicted surface composition and thermodynamic stability of MXenes in solution, *J. Phys. Chem. C* 120 (2016) 3550–3556, <https://doi.org/10.1021/acs.jpcc.5b11887>.
- [79] Q. Meng, J. Ma, Y. Zhang, Z. Li, C. Zhi, A. Hu, J. Fan, The S-functionalized Ti_3C_2 MXene as a high capacity electrode material for Na-ion batteries: a DFT study, *Nanoscale* 10 (2018) 3385–3392, <https://doi.org/10.1039/c7nr07649e>.
- [80] M.R. Lukatskaya, O. Mashtalir, C.E. Ren, Y. Dall’Agnese, P. Rozier, P.L. Taberna, M. Naguib, P. Simon, M.W. Barsoum, Y. Gogotsi, Cation intercalation and high volumetric capacitance of two-dimensional titanium carbide, *Science* 341 (2013) 1502–1505, <https://doi.org/10.1126/science.1241488>.
- [81] A.M. Navarro-Suárez, K. Maleski, T. Makaryan, J. Yan, B. Anasori, Y. Gogotsi, 2D titanium carbide/reduced graphene oxide heterostructures for supercapacitor applications, *Batter. Supercaps.* 1 (2018) 33–38, <https://doi.org/10.1002/batt.201800014>.
- [82] A.S. Levitt, M. Alhabeb, C.B. Hatter, A. Sarycheva, G. Dion, Y. Gogotsi, Electrospun MXene/carbon nanofibers as supercapacitor electrodes, *J. Mater. Chem. A* 7 (2019) 269–277, <https://doi.org/10.1039/c8ta09810g>.
- [83] J. Yan, C.E. Ren, K. Maleski, C.B. Hatter, B. Anasori, P. Urbankowski, A. Sarycheva, Y. Gogotsi, Flexible MXene/graphene films for ultrafast supercapacitors with outstanding volumetric capacitance, *Adv. Funct. Mater.* 27 (2017) 1701264, <https://doi.org/10.1002/adfm.201701264>.
- [84] Y. Dall’Agnese, M.R. Lukatskaya, K.M. Cook, P.L. Taberna, Y. Gogotsi, P. Simon, High capacitance of surface-modified 2D titanium carbide in acidic electrolyte, *Electrochem. Commun.* 48 (2014) 118–122, <https://doi.org/10.1016/j.elecom.2014.09.002>.
- [85] Z. Wang, S. Qin, S. Seyedin, J. Zhang, J. Wang, A. Levitt, N. Li, C. Haines, R. Ovalle-Robles, W. Lei, Y. Gogotsi, R.H. Baughman, J.M. Razal, High-performance bistructured MXene/carbon nanotube yarn supercapacitors, *Small* 14 (2018) 1802225, <https://doi.org/10.1002/smll.201802225>.
- [86] L. Yu, L. Hu, B. Anasori, Y.T. Liu, Q. Zhu, P. Zhang, Y. Gogotsi, B. Xu, MXene-bonded activated carbon as a flexible electrode for high-performance supercapacitors, *ACS Energy Lett* 3 (2018) 1597–1603, <https://doi.org/10.1021/acsenenergylett.8b00718>.
- [87] M. Boota, B. Anasori, C. Voigt, M.Q. Zhao, M.W. Barsoum, Y. Gogotsi, Pseudocapacitive electrodes produced by oxidant-free polymerization of pyrrole between the layers of 2D titanium carbide (MXene), *Adv. Mater.* 28 (2016) 1517–1522, <https://doi.org/10.1002/adma.201504705>.
- [88] Q. Fu, X. Wang, N. Zhang, J. Wen, L. Li, H. Gao, X. Zhang, Self-assembled $\text{Ti}_3\text{C}_2\text{T}_x/\text{SCNT}$ composite electrode with improved electrochemical performance for supercapacitor, *J. Colloid Interface Sci.* 511 (2018) 128–134, <https://doi.org/10.1016/j.jcis.2017.09.104>.
- [89] L. Wang, H. Zhang, B. Wang, C. Shen, C. Zhang, Q. Hu, A. Zhou, B. Liu, Synthesis and electrochemical performance of $\text{Ti}_3\text{C}_2\text{T}_x$ with hydrothermal process,

- Electron. Mater. Lett. 12 (2016) 702–710, <https://doi.org/10.1007/s13391-016-6088-z>.
- [90] C. Zhao, Q. Wang, H. Zhang, S. Passerini, X. Qian, Two-dimensional titanium carbide/RGO composite for high-performance supercapacitors, *ACS Appl. Mater. Interfaces* 8 (2016) 15661–15667, <https://doi.org/10.1021/acsami.6b04767>.
- [91] R.B. Rakhi, B. Ahmed, M.N. Hedhili, D.H. Anjum, H.N. Alshareef, Effect of postetch annealing gas composition on the structural and electrochemical properties of Ti_2CT_x MXene electrodes for supercapacitor applications, *Chem. Mater.* 27 (2015) 5314–5323, <https://doi.org/10.1021/acs.chemmater.5b01623>.
- [92] Q. Tao, M. Dahlqvist, J. Lu, S. Kota, R. Meshkian, J. Halim, J. Palisaitis, L. Hultman, M.W. Barsoum, P.O.Å. Persson, J. Rosen, Two-dimensional $\text{Mo}_{1.33}\text{C}$ MXene with divacancy ordering prepared from parent 3D laminate with in-plane chemical ordering, *Nat. Commun.* 8 (2017) 14949, <https://doi.org/10.1038/ncomms14949>.
- [93] J. Halim, S. Kota, M.R. Lukatskaya, M. Naguib, M.Q. Zhao, E.J. Moon, J. Pitock, J. Nanda, S.J. May, Y. Gogotsi, M.W. Barsoum, Synthesis and characterization of 2D molybdenum carbide (MXene), *Adv. Funct. Mater.* 26 (2016) 3118–3127, <https://doi.org/10.1002/adfm.201505328>.
- [94] Q. Shan, X. Mu, M. Alhabeb, C.E. Shuck, D. Pang, X. Zhao, X.F. Chu, Y. Wei, F. Du, G. Chen, Y. Gogotsi, Y. Gao, Y. Dall'Agnese, Two-dimensional vanadium carbide (V_2C) MXene as electrode for supercapacitors with aqueous electrolytes, *Electrochem. Commun.* 96 (2018) 103–107, <https://doi.org/10.1016/j.elecom.2018.10.012>.
- [95] O. Mashtalir, M.R. Lukatskaya, M.Q. Zhao, M.W. Barsoum, Y. Gogotsi, Amine-assisted delamination of Nb_2C MXene for Li-ion energy storage devices, *Adv. Mater.* 27 (2015) 3501–3506, <https://doi.org/10.1002/adma.201500604>.
- [96] M.R. Lukatskaya, S.-M. Bak, X. Yu, X.-Q. Yang, M.W. Barsoum, Y. Gogotsi, Probing the mechanism of high capacitance in 2D titanium carbide using in situ X-ray absorption spectroscopy, *Adv. Energy Mater.* 5 (2015) 1500589, <https://doi.org/10.1002/aenm.201500589>.
- [97] K. Maleski, C.E. Ren, M.Q. Zhao, B. Anasori, Y. Gogotsi, Size-dependent physical and electrochemical properties of two-dimensional MXene flakes, *ACS Appl. Mater. Interfaces* 10 (2018) 24491–24498, <https://doi.org/10.1021/acsami.8b04662>.
- [98] P. Nayak, Q. Jiang, R. Mohanraman, D. Anjum, M.N. Hedhili, H.N. Alshareef, Inherent electrochemistry and charge transfer properties of few-layered two-dimensional $\text{Ti}_3\text{C}_2\text{Tx}$ MXene, *Nanoscale* 10 (2018) 17030–17037, <https://doi.org/10.1039/c8nr01883a>.
- [99] J. Tang, T.S. Mathis, N. Kurra, A. Sarycheva, C. Hatter, X. Xiao, Tuning the electrochemical performance of titanium carbide MXene by controllable in situ anodic oxidation, *Angew. Chem. Int. Ed.* 58 (2019) 2–9, <https://doi.org/10.1002/anie.201911604>.
- [100] J.P. Equilibría, J.D. Béguin, J. Alexis, T. Masri, Weldability of superalloys Hastelloy X by Yb : YAG laser, *Adv. Mater. Res.* 508 (2006) 621–628, <https://doi.org/10.4028/www.scientific.net/MSF.508.621>.
- [101] Z. Lin, D. Barbara, P.L. Taberna, K.L. Van Aken, B. Anasori, Y. Gogotsi, P. Simon, Capacitance of $\text{Ti}_3\text{C}_2\text{Tx}$ MXene in ionic liquid electrolyte, *J. Power Sources* 326 (2016) 575–579, <https://doi.org/10.1016/j.jpowsour.2016.04.035>.
- [102] X. Wang, T.S. Mathis, K. Li, Z. Lin, L. Vleck, T. Torita, N.C. Osti, C. Hatter, P. Urbankowski, A. Sarycheva, M. Tyagi, E. Mamontov, P. Simon, Y. Gogotsi, Influences from solvents on charge storage in titanium carbide MXenes, *Nat. Energy* 4 (2019) 241–248, <https://doi.org/10.1038/s41560-019-0339-9>.
- [103] S. Kajiyama, L. Szabova, H. Iinuma, A. Sugahara, K. Gotoh, K. Sodeyama, Y. Tateyama, M. Okubo, A. Yamada, Enhanced Li-ion accessibility in MXene titanium carbide by steric chloride termination, *Adv. Energy Mater.* 7 (2017) 1601873, <https://doi.org/10.1002/aenm.201601873>.
- [104] Y. Dall'Agnese, P. Rozier, P.L. Taberna, Y. Gogotsi, P. Simon, Capacitance of two-dimensional titanium carbide (MXene) and MXene/carbon nanotube composites in organic electrolytes, *J. Power Sources* 306 (2016) 510–515, <https://doi.org/10.1016/j.jpowsour.2015.12.036>.
- [105] S. Zheng, C. Zhang, F. Zhou, Y. Dong, X. Shi, V. Nicolosi, Z.S. Wu, X. Bao, Ionic liquid pre-intercalated MXene films for ionogel-based flexible micro-supercapacitors with high volumetric energy density, *J. Mater. Chem. A* 7 (2019) 9478–9485, <https://doi.org/10.1039/c9ta02190f>.
- [106] Q. Jiang, N. Kurra, K. Maleski, Y. Lei, H. Liang, Y. Zhang, Y. Gogotsi, H.N. Alshareef, On-chip MXene micro-supercapacitors for AC-line filtering applications, *Adv. Energy Mater.* 9 (2019) 1901061, <https://doi.org/10.1002/aenm.201901061>.
- [107] S. Xu, W. Liu, X. Liu, X. Kuang, X. Wang, A MXene based all-solid-state micro-supercapacitor with 3D interdigital electrode, *Transducer* 27 (2017) 18–22, <https://doi.org/10.1109/TRANSDUCERS.2017.7994146>.
- [108] C. Lethien, J. LE Bideau, T. Brousse, Challenges and prospects of 3D micro-supercapacitors for powering the Internet of Things, *Energy Environ. Sci.* 12 (2019) 95–115, <https://doi.org/10.1039/C8EE02029A>.
- [109] S. Xu, G. Wei, J. Li, Y. Ji, N. Klyui, V. Izotov, W. Han, Binder-free $\text{Ti}_3\text{C}_2\text{Tx}$ MXene electrode film for supercapacitor produced by electrophoretic deposition method, *Chem. Eng. J.* 317 (2017) 1026–1036, <https://doi.org/10.1016/j.cej.2017.02.144>.
- [110] P. Collini, S. Kota, A.D. Dillon, M.W. Barsoum, A.T. Fafarman, Electrophoretic deposition of two-dimensional titanium carbide (MXene) thick films, *J. Electrochem. Soc.* 164 (2017) 573–580, <https://doi.org/10.1149/2.0211709jes>.
- [111] L. Yang, W. Zheng, P. Zhang, J. Chen, W.B. Tian, Y.M. Zhang, Z.M. Sun, MXene/CNTs films prepared by electrophoretic deposition for supercapacitor electrodes, *J. Electroanal. Chem.* 830–831 (2018) 1–6, <https://doi.org/10.1016/j.jelechem.2018.10.024>.
- [112] L. Qin, Q. Tao, X. Liu, M. Fahlman, J. Halim, P.O.Å. Persson, J. Rosen, F. Zhang, Polymer-MXene composite films formed by MXene-facilitated electrochemical polymerization for flexible solid-state micro-supercapacitors, *Nano Energy* 60 (2019) 734–742, <https://doi.org/10.1016/j.nanoen.2019.04.002>.
- [113] Y.Y. Peng, B. Akuzum, N. Kurra, M.Q. Zhao, M. Alhabeb, B. Anasori, E.C. Kumbur, H.N. Alshareef, M. Der Ger, Y. Gogotsi, All-MXene (2D titanium carbide) solid-state micro-supercapacitors for on-chip energy storage, *Energy Environ. Sci.* 9 (2016) 2847–2854, <https://doi.org/10.1039/c6ee01717g>.
- [114] N. Kurra, B. Ahmed, Y. Gogotsi, H.N. Alshareef, MXene-on-paper coplanar micro-supercapacitors, *Adv. Energy Mater.* 6 (2016) 1601372, <https://doi.org/10.1002/aenm.201601372>.
- [115] S. Jiao, A. Zhou, M. Wu, H. Hu, Kirigami patterning of MXene/bacterial Cellulose composite paper for all-solid-state stretchable micro-supercapacitor arrays, *Adv. Sci.* 6 (2019) 1900529, <https://doi.org/10.1002/advs.201900529>.
- [116] Y. Yue, N. Liu, Y. Ma, S. Wang, W. Liu, C. Luo, H. Zhang, F. Cheng, J. Rao, X. Hu, J. Su, Y. Gao, Highly self-healable 3D micro-supercapacitor with MXene-graphene composite aerogel, *ACS Nano* 12 (2018) 4224–4232, <https://doi.org/10.1021/acsnano.7b07528>.
- [117] H. Huang, H. Su, H. Zhang, L. Xu, X. Chu, C. Hu, H. Liu, N. Chen, F. Liu, W. Deng, B. Gu, H. Zhang, W. Yang, Extraordinary areal and volumetric performance of flexible solid-state micro-supercapacitors based on highly conductive freestanding $\text{Ti}_3\text{C}_2\text{Tx}$ films, *Adv. Electron. Mater.* 4 (2018) 1800179, <https://doi.org/10.1002/aelm.201800179>.
- [118] J. Kim, R. Kumar, A.J. Bandodkar, J. Wang, Advanced materials for printed wearable electrochemical devices: a review, *Adv. Electron. Mater.* 3 (2017) 1600260, <https://doi.org/10.1002/aelm.201600260>.
- [119] H. Li, J. Liang, Recent development of printed micro-supercapacitors: printable materials, printing technologies, and perspectives, *Adv. Mater.* (2019) 1805864, <https://doi.org/10.1002/adma.201805864>.
- [120] H. Li, X. Li, J. Liang, Y. Chen, Hydrous RuO_2 -decorated MXene coordinating with silver nanowire links enabling fully printed micro-supercapacitors with extraordinary volumetric performance, *Adv. Energy Mater.* 9 (2019) 1803987, <https://doi.org/10.1002/aenm.201803987>.
- [121] S. Xu, Y. Dall'Agnese, G. Wei, C. Zhang, Y. Gogotsi, W. Han, Screen-printable microscale hybrid device based on MXene and layered double hydroxide electrodes for powering force sensors, *Nano Energy* 50 (2018) 479–488, <https://doi.org/10.1016/j.nanoen.2018.05.064>.
- [122] B. Derby, Inkjet printing of functional and structural materials: fluid property requirements, feature stability, and resolution, *Annu. Rev. Mater. Res.* 40 (2010) 395–414, <https://doi.org/10.1146/annurev-matsci-070909-104502>.
- [123] H. Sirringhaus, T. Kawase, R.H. Friend, T. Shimoda, High-Resolution Inkjet Printing of All-Polymer Transistor Circuits 290 (2000) 2123–2127.
- [124] T. Aernouts, T. Aleksandrov, C. Girotto, J. Genoe, J. Poortmans, Polymer based organic solar cells using ink-jet printed active layers, *Appl. Phys. Lett.* 92 (2008), 033306, <https://doi.org/10.1063/1.2833185>.
- [125] T.R. Hebrer, C.C. Wu, D. Marcy, M.H. Lu, J.C. Sturm, Ink-jet printing of doped polymers for organic light emitting devices, *Appl. Phys. Lett.* 72 (1998) 519, <https://doi.org/10.1063/1.120807>.
- [126] Y. Noguchi, T. Sekitani, T. Someya, Organic-transistor-based flexible pressure sensors using ink-jet-printed electrodes and gate dielectric layers, *Appl. Phys. Lett.* 89 (2006) 253507, <https://doi.org/10.1063/1.2416001>.
- [127] R.D. Boehm, P.R. Miller, J. Daniels, S. Stafslien, R.J. Narayan, Inkjet printing for pharmaceutical applications, *Biochem. Pharmacol.* 17 (2014) 247–252, <https://doi.org/10.1016/j.mattod.2014.04.027>.
- [128] N. Reis, B. Derby, Ink jet deposition of ceramic suspensions: modeling and experiments of droplet formation, *Mater. Res.* 625 (2000) 117–122, <https://doi.org/10.1557/PROC-625-117>.
- [129] C.D. Stow, M.G. Hadfield, An experimental investigation of fluid flow resulting from the impact of a water drop with an unyielding dry surface, *Proc. R. Soc. Lond.* 373 (1981) 419–441, <https://doi.org/10.1098/rspa.1981.0002>.
- [130] B. Akuzum, K. Maleski, B. Anasori, P. Lelyukh, N.J. Alvarez, E.C. Kumbur, Y. Gogotsi, Rheological characteristics of 2D titanium carbide (MXene) dispersions: a guide for processing MXenes, *ACS Nano* 12 (2018) 2685–2694, <https://doi.org/10.1021/acsnano.7b08889>.
- [131] C.F. Zhang, L. McKeon, M.P. Kremer, S.H. Park, O. Ronan, A. Seral-Ascaso, S. Barwich, C. Coileáin, N. McEvoy, H.C. Nerl, B. Anasori, J.N. Coleman, Y. Gogotsi, V. Nicolosi, Additive-free MXene inks and direct printing of micro-supercapacitors, *Nat. Commun.* 10 (2019) 1795, <https://doi.org/10.1038/s41467-019-09398-1>.
- [132] E. Quain, T.S. Mathis, N. Kurra, K. Maleski, K.L. Van Aken, M. Alhabeb, H.N. Alshareef, Y. Gogotsi, Direct writing of additive-free MXene-in-water ink for electronics and energy storage, *Adv. Mater. Technol.* 4 (2019) 1800256, <https://doi.org/10.1002/admt.201800256>.
- [133] C. Zhang, M.P. Kremer, A. Seral-Ascaso, S.H. Park, N. McEvoy, V. Nicolosi, B. Anasori, Y. Gogotsi, V. Nicolosi, Stamping of flexible, coplanar micro-supercapacitors using MXene inks, *Adv. Funct. Mater.* 28 (2018) 1705506, <https://doi.org/10.1002/adfm.201705506>.
- [134] H. Hu, Z. Bai, B. Niu, M. Wu, T. Hua, Binder-free bonding of modularized MXene thin films into thick film electrodes for on-chip micro-supercapacitors with enhanced areal performance metrics, *J. Mater. Chem. A* 6 (2018) 14876–14884, <https://doi.org/10.1039/c8ta04737e>.
- [135] H. Li, Y. Hou, F. Wang, M.R. Lohe, X. Zhuang, L. Niu, X. Feng, Flexible all-solid-state supercapacitors with high volumetric capacitances boosted by solution processable MXene and electrochemically exfoliated graphene, *Adv. Energy Mater.* 7 (2017) 1601847, <https://doi.org/10.1002/aenm.201601847>.

- [136] Q. Jiang, C. Wu, Z.J. Wang, A.C. Wang, J.H. He, Z.L. Wang, H.N. Alshareef, MXene electrochemical microsupercapacitor integrated with triboelectric nanogenerator as a wearable self-charging power unit, *Nano Energy* 45 (2018) 266–272, <https://doi.org/10.1016/j.nanoen.2018.01.004>.
- [137] H. Hu, T. Hua, An easily manipulated protocol for patterning of MXenes on paper for planar micro-supercapacitors, *J. Mater. Chem. A* 5 (2017) 19639–19648, <https://doi.org/10.1039/c7ta04735e>.
- [138] B.S. Shen, H. Wang, L.J. Wu, R.S. Guo, Q. Huang, X. Bin Yan, All-solid-state flexible microsupercapacitor based on two-dimensional titanium carbide, *Chin. Chem. Lett.* 27 (2016) 1586–1591, <https://doi.org/10.1016/j.ccl.2016.04.012>.
- [139] P. Salles, E. Quain, N. Kurra, A. Sarycheva, Y. Gogotsi, Automated scalpel patterning of solution processed thin films for fabrication of transparent MXene microsupercapacitors, *Small* 14 (2018) 1802864, <https://doi.org/10.1002/smll.201802864>.
- [140] P. Li, W. Shi, W. Liu, Y. Chen, X. Xu, S. Ye, R. Yin, L. Zhang, L. Xu, X. Cao, Fabrication of high-performance MXene-based all-solid-state flexible microsupercapacitor based on a facile scratch method, *Nanotechnology* 29 (2018) 445401, <https://doi.org/10.1088/1361-6528/aad4d4>.
- [141] J. Li, A. Levitt, N. Kurra, K. Juan, N. Noriega, X. Xiao, X. Wang, H. Wang, H.N. Alshareef, Y. Gogotsi, MXene-conducting polymer electrochromic microsupercapacitors, *Energy Storage Mater* 20 (2019) 455–461, <https://doi.org/10.1016/j.ensm.2019.04.028>.
- [142] N. Wang, J. Liu, Y. Zhao, M. Hu, R. Qin, G. Shan, Laser-cutting fabrication of mxene-based flexible micro-supercapacitors with high areal capacitance, *ChemNanoMat* 5 (2019) 658–665, <https://doi.org/10.1002/cnma.201800674>.
- [143] C. Couly, M. Alhabeb, K.L. Van Aken, N. Kurra, L. Gomes, A.M. Navarro-Suárez, B. Anasori, H.N. Alshareef, Y. Gogotsi, Asymmetric flexible MXene-reduced graphene oxide micro-supercapacitor, *Adv. Electron. Mater.* 4 (2018) 1700339, <https://doi.org/10.1002/aeml.201700339>.
- [144] H. Xiao, Z.S. Wu, L. Chen, F. Zhou, S. Zheng, W. Ren, H.M. Cheng, X. Bao, One-step device fabrication of phosphorene and graphene interdigital micro-supercapacitors with high energy density, *ACS Nano* 11 (2017) 7284–7292, <https://doi.org/10.1021/acsnano.7b03288>.
- [145] S. Zheng, J. Ma, Z.S. Wu, F. Zhou, Y.B. He, F. Kang, H.M. Cheng, X. Bao, All-solid-state flexible planar lithium ion micro-capacitors, *Energy Environ. Sci.* 11 (2018), <https://doi.org/10.1039/c8ee00855h>, 2001–2009.
- [146] M. Hu, Z. Li, G. Li, T. Hu, C. Zhang, X. Wang, All-solid-state flexible fiber-based MXene supercapacitors, *Adv. Mater. Technol.* 2 (2017) 1700143, <https://doi.org/10.1002/admt.201700143>.
- [147] M. Hu, T. Hu, R. Cheng, J. Yang, C. Cui, C. Zhang, X. Wang, MXene-coated silk-derived carbon cloth toward flexible electrode for supercapacitor application, *J. Energy Chem.* 27 (2018) 161–166, <https://doi.org/10.1016/j.jechem.2017.10.030>.
- [148] W. Shao, M. Tebyetekerwa, I. Marriam, W. Li, Y. Wu, S. Peng, S. Ramakrishna, S. Yang, M. Zhu, Polyester@MXene nanofibers-based yarn electrodes, *J. Power Sources* 396 (2018) 683–690, <https://doi.org/10.1016/j.jpowsour.2018.06.084>.
- [149] Q. Yang, Z. Xu, B. Fang, T. Huang, S. Cai, H. Chen, Y. Liu, K. Gopalsamy, W. Gao, C. Gao, MXene/graphene hybrid fibers for high performance flexible supercapacitors, *J. Mater. Chem. A* 5 (2017) 22113–22119, <https://doi.org/10.1039/C7TA07999K>.
- [150] J. Zhang, S. Seyedin, Z. Gu, W. Yang, X. Wang, J.M. Razal, MXene, A potential candidate for yarn supercapacitors, *Nanoscale* 9 (2017) 18604–18608, <https://doi.org/10.1039/c7nr06619h>.
- [151] C. Yu, Y. Gong, R. Chen, M. Zhang, J. Zhou, J. An, F. Lv, S. Guo, G. Sun, A solid-state fibriform supercapacitor boosted by host–guest hybridization between the carbon nanotube scaffold and MXene nanosheets, *Small* 14 (2018) 1801203, <https://doi.org/10.1002/smll.201801203>.
- [152] Z. Wang, X. Chu, Z. Xu, H. Su, C. Yan, F. Liu, B. Gu, H. Huang, D. Xiong, H. Zhang, W. Deng, H. Zhang, W. Yang, Extremely low self-discharge solid-state supercapacitors: via the confinement effect of ion transfer, *J. Mater. Chem. A* 7 (2019) 8633–8640, <https://doi.org/10.1039/c9ta01028a>.
- [153] M. Xia, J. Nie, Z. Zhang, X. Lu, Z.L. Wang, Suppressing self-discharge of supercapacitors via electrochemical effect of liquid crystals, *Nano Energy* 47 (2018) 43–50, <https://doi.org/10.1016/j.nanoen.2018.02.022>.
- [154] H.A. Andreas, Self-discharge in electrochemical capacitors: a perspective article, *J. Electrochem. Soc.* 162 (2015) 5047–5053, <https://doi.org/10.1149/2.0081505jes>.
- [155] B.E. Conway, W.G. Pell, T.C. Liu, Diagnostic analyses for mechanisms of self-discharge of electrochemical capacitors and batteries, *J. Power Sources* 65 (1997) 53–59, [https://doi.org/10.1016/S0378-7753\(97\)02468-3](https://doi.org/10.1016/S0378-7753(97)02468-3).
- [156] I.S. Ike, I. Sigalas, S. Iyuke, Understanding performance limitation and suppression of leakage current or self-discharge in electrochemical capacitors: a review, *Phys. Chem. Chem. Phys.* 18 (2015) 661–680, <https://doi.org/10.1039/c5cp05459a>.
- [157] A. Lewandowski, P. Jakobczyk, M. Galinski, M. Biegun, Capacitance of electrochemical double layer capacitors, *Electrochim. Acta* 86 (2013) 225–231, <https://doi.org/10.1039/c3cp44612c>.
- [158] J. Duay, E. Gillette, R. Liu, S.B. Lee, Highly flexible pseudocapacitor based on freestanding heterogeneous MnO₂/conductive polymer nanowire arrays, *Phys. Chem. Chem. Phys.* 14 (2012) 3329–3337, <https://doi.org/10.1039/c2cp00019a>.
- [159] C.W. Huang, C.A. Wu, S.S. Hou, P.L. Kuo, C. Te Hsieh, H. Teng, Gel electrolyte derived from poly(ethylene glycol) blending poly(acrylonitrile) applicable to roll-to-roll assembly of electric double layer capacitors, *Adv. Funct. Mater.* 22 (2012) 4677–4685, <https://doi.org/10.1002/adfm.201201342>.
- [160] R. Yuksel, Z. Sarioba, A. Cirpan, P. Hiralal, H.E. Unalan, Transparent and flexible supercapacitors with single walled carbon nanotube thin film electrodes, *ACS Appl. Mater. Interfaces* 6 (2014) 15434–15439, <https://doi.org/10.1021/am504021u>.
- [161] Y. Lim, J. Yoon, J. Yun, D. Kim, S.Y. Hong, S.J. Lee, G. Zi, J.S. Ha, Biaxially stretchable, integrated array of high performance microsupercapacitors, *ACS Nano* 8 (2014) 11639–11650, <https://doi.org/10.1021/nn504925s>.
- [162] C.W. Liew, S. Ramesh, A.K. Arof, Good prospect of ionic liquid based-poly(vinyl alcohol) polymer electrolytes for supercapacitors with excellent electrical, electrochemical and thermal properties, *Int. J. Hydrogen Energy* 39 (2014) 2953–2963, <https://doi.org/10.1016/j.ijhydene.2013.06.061>.
- [163] J. Zheng, X. Li, Y. Yu, X. Zhen, Y. Song, X. Feng, Y. Zhao, Cross-linking copolymers of acrylates' gel electrolytes with high conductivity for lithium-ion batteries, *J. Solid State Electrochem.* 18 (2014), <https://doi.org/10.1007/s10008-014-2438-7>, 2013–2018.
- [164] N. Kurra, M. Alhabeb, K. Maleski, C.H. Wang, H.N. Alshareef, Y. Gogotsi, Bistacked titanium carbide (MXene) anodes for hybrid sodium-ion capacitors, *ACS Energy Lett* 3 (2018) 2094–2100, <https://doi.org/10.1021/acsenergylett.8b01062>.
- [165] M.Q. Zhao, C.E. Ren, Z. Ling, M.R. Lukatskaya, C. Zhang, K.L. Van Aken, M.W. Barsoum, Y. Gogotsi, Flexible MXene/carbon nanotube composite paper with high volumetric capacitance, *Adv. Mater.* 27 (2015) 339–345, <https://doi.org/10.1002/adma.201404140>.
- [166] A. Vahidmohammadi, J. Moncada, H. Chen, E. Kayali, J. Orangi, C.A. Carrero, M. Beidaghi, Thick and freestanding MXene/PANI pseudocapacitive electrodes with ultrahigh specific capacitance, *J. Mater. Chem. A* 6 (2018) 22123–22133, <https://doi.org/10.1039/c8ta05807e>.
- [167] J. Yan, Y. Ma, C. Zhang, X. Li, W. Liu, X. Yao, S. Yao, S. Luo, Polypyrrole-MXene coated textile-based flexible energy storage device, *RSC Adv.* 8 (2018) 39742–39748, <https://doi.org/10.1039/c8ra08403c>.
- [168] H. Li, X. Li, J. Liang, Y. Chen, Hydrous RuO₂-decorated MXene coordinating with silver nanowire inks enabling fully printed micro-supercapacitors with extraordinary volumetric performance, *Adv. Energy Mater.* 9 (2019) 1803987, <https://doi.org/10.1002/aenm.201803987>.
- [169] Y. Xia, T.S. Mathis, M.Q. Zhao, B. Anasori, A. Dang, Z. Zhou, H. Cho, Y. Gogotsi, S. Yang, Thickness-independent capacitance of vertically aligned liquid-crystalline MXenes, *Nature* 557 (2018) 409–412, <https://doi.org/10.1038/s41586-018-0109-z>.
- [170] Q. Xue, H. Zhang, M. Zhu, Z. Pei, H. Li, Z. Wang, Y. Huang, Y. Huang, Q. Deng, J. Zhou, S. Du, Q. Huang, C. Zhi, Photoluminescent Ti₃C₂ MXene quantum dots for multicolor cellular imaging, *Adv. Mater.* 29 (2017) 1604847, <https://doi.org/10.1002/adma.201604847>.
- [171] X. Chen, X. Sun, W. Xu, G. Pan, D. Zhou, J. Zhu, H. Wang, X. Bai, B. Dong, H. Song, Ratiometric photoluminescence sensing based on Ti₃C₂ MXene quantum dots as an intracellular pH sensor, *Nanoscale* 10 (2018) 1111–1118, <https://doi.org/10.1039/c7nr06958h>.
- [172] X. Yu, X. Cai, H. Cui, S.W. Lee, X.F. Yu, B. Liu, Fluorine-free preparation of titanium carbide MXene quantum dots with high near-infrared photothermal performances for cancer therapy, *Nanoscale* 9 (2017) 17859–17864, <https://doi.org/10.1039/c7nr05997c>.